An Observational Study of Cloud-Topped Mixed Layers

BRUCE A. ALBRECHT AND RICHARD S. PENC[1]

The Pennsylvania State University, University Park, PA 16802

WAYNE H. SCHUBERT

Colorado State University, Ft. Collins, CO 80521

(Manuscript received 3 October 1984, in final form 10 December 1984)

ABSTRACT

The turbulence and mean structure of oceanic stratocumulus was studied using aircraft data collected during the summer of 1976 off the coast of California. Three cloud-topped mixed layers were studied in detail. They consisted of 1) a thin cloud capped by an inversion at a height of ~1000 m, 2) a relatively thick but broken cloud layer capped by a weak inversion at ~600 m and 3) a solid cloud capped by a strong inversion at ~600 m. The mean temperature, moisture, liquid water and radiative characteristics obtained for these three cases were compared. Heat and moisture fluxes were also calculated and compared.

Although there was considerable variation in the characteristics of the three cloud-topped mixed layers studied, all indicated the validity of the general approach used in simple mixed-layer models of stratocumulus. But for these models to be useful, they should be generalized to allow clouds other than solid clouds to be modeled. The measurements indicate that cloud microphysics may be important in regulating the structure of stratocumulus clouds and that the cloud structure is important in regulating the distribution of radiative cooling. The thin cloud case satisfied conditions for cloud-top entrainment instability, but no evidence of enhanced entrainment was observed. In the analysis it is shown that this cloud may have had insufficient liquid water available to drive the instability. Restrictions on cloud-top entrainment instability criteria are discussed, and it is shown that the instability may be neither a necessary nor a sufficient condition for the breakup of stratocumulus.

1. Introduction

Stratocumulus clouds are frequently observed over eastern regions of the oceans. These clouds significantly affect the surface heat budget and may be important in regulating the earth's climate.

Because of the possible importance of these clouds, there has been considerable theoretical work on stratocumulus convection. This work has primarily been on aspects of the cloud-topped mixed layer model described by Lilly (1968). Variations or applications of this model are described by Schubert (1976), Deardorff (1976), Kraus and Schaller (1978a,b), Schubert *et al.* (1979a,b), Schaller and Kraus (1978, 1981a,b), Randall (1980a), Wakefield and Schubert (1981), Fravalo *et al.* (1981), and others. A somewhat different approach is described by Stage and Businger (1981a,b).

The physics in the mixed-layer models is reduced to the application of appropriate heat and moisture budgets, a parameterization of the exchange of heat and moisture at the air–sea interface, the parameterization of radiative effects and the parameterization of the rate at which mass is entrained into the boundary layer at the inversion. Many of the theoretical studies have focused on entrainment and radiative effects. However, since a simple mixed-layer structure is assumed in these models and the convective fluxes are obtained implicitly by the closure assumptions, it is not clear whether the differences between the various models are conceptual or have more practical implications.

In addition, studies of stratus have been made using second-order closure techniques (Oliver *et al.*, 1978; Moeng and Arakawa, 1980; Chen and Cotton, 1983) and a three-dimensional model has been used to test assumptions made in simple mixed-layer models (Deardorff, 1980b).

Other studies have been made of the instability that may occur when unsaturated air above the inversion mixes with saturated air in the cloud layer (Lilly, 1968; Randall, 1980b; Deardorff, 1980a). Under the proper conditions this mixture may be negatively buoyant, forcing vertical mixing and entrainment at the inversion. This process has been suggested as a mechanism for the breakup of stratocumulus clouds.

Although there have been numerous theoretical and modeling studies of stratocumulus, there have been few observational studies. Brost *et al.* (1982a,b)

[1] Present affiliation: Research Data Systems, NASA Goddard Space Center, Greenbelt, MD 20771.

analyzed data collected off the coast of California in 1976 from the NCAR Electra. A description of the flight patterns and the data collected during this experiment is given in Wakefield and Schubert (1976). Brost *et al.* (1982a,b) used these data to demonstrate some of the shortcomings of the simple mixed-layer models. They obtained mean conditions for stratocumulus observed on two days and calculated turbulence kinetic energy budgets for these cases; the possible role of shear production was demonstrated. Roach *et al.* (1982), Caughey *et al.* (1982), and Slingo *et al.* (1982) studied stratocumulus over Great Britain by obtaining the mean and turbulence structure and the radiative and microphysical properties from an instrumented tethered balloon. Hanson (1984a) used soundings obtained in stratocumulus clouds off the coast of California to study their structure within the framework of a saturation-point analysis (Betts, 1982). Noonkester (1984) made detailed measurements of droplet spectra in stratus cloud layers southwest of San Diego.

In this paper, data collected during the 1976 Electra flights described by Wakefield and Schubert (1976) and Brost *et al.* are used to compare the mean structure, heat, moisture, and radiative fluxes, and the cloud microphysics structure of three cloud-topped mixed layers with different cloud characteristics. Only the thermodynamic structure and fluxes of thermodynamic quantities will be discussed. Kinetic energy budgets for the clouds observed on 13 and 17 June 1976 are presented by Brost *et al.* (1982b). The parametric representation of stratocumulus fluxes, proposed by Betts (1978, 1983), has been tested in the work of Penc (1983).

2. Synoptic conditions

Five flights were made in June 1976 during the stratocumulus experiment described in Section 1. However, well-defined turbulent mixed layers were observed on only three of these flights. Although the mixed layers observed on these flights were cloud topped, the characteristics of these clouds varied. The clouds observed on these flights will be classified as "thin" (5 June 1976), "broken" (13 June 1976), and "solid" (17 June 1976). Further evidence for these distinctions will be given.

On the 5 June 1976 flight, measurements were made in a mixed layer with a relatively *thin* (<200 m thick) cloud layer. The visible GOES-West satellite photograph presented in Fig. 1a shows the cloud features on this day and the approximate location of the area where the measurements were made. The clouds in the area of interest have a cellular appearance, with relatively large broken areas to the west of the region where the measurements were made.

The 1200 GMT surface weather map for this date (Fig. 1b) shows low pressure over the southwestern United States and high pressure to the northwest. This pressure pattern is consistent with the northwesterly winds observed in the boundary layer on this day. The position of the 500 mb trough is indicated in Fig. 1b and is west of the surface low. A 500 mb ridge is located west of the surface high pressure in the northern Pacific.

On the 13 June 1976 flight, measurements were made in a cloud that extended over most of the depth of the boundary layer. Although this cloud is relatively deep, it has a broken structure. The satellite photograph (Fig. 2a) shows that the cloud has a relatively tenuous character over a considerable area to the west of the observational area. A large clear area is located to the east of the area studied.

The surface map (Fig. 2b) shows that the clearing off the coast may be due to the passage of a weak front; this area of clearing increased during the day. The surface maps for this day show a relatively well defined low-pressure system in southern Canada and a high centered off the coast of northern California.

On the 17 June 1976 flight, measurements were made in a relatively solid stratocumulus deck. The satellite photograph for this case (Fig. 3a) shows an extensive cloud deck over most of the eastern Pacific. Compared to the satellite photographs for the 5 June and 13 June flights, this photograph shows little small-scale structure. On the surface map (Fig. 3a) a trough extends through the Great Plains and high pressure is observed over northern California. A relatively strong surface pressure gradient is in the area where the measurements were made and strong northerly winds were observed in the boundary layer in this region (Brost *et al.*, 1982a). The 500 mb flow shows upper-level support for the surface features with the trough and ridge being farther east than they were on 5 June. The upper-level flow is similar to the flow on 13 June with the ridge and trough locations slightly east of the 13 June locations.

Although Brost *et al.* (1982a) show that strong winds are a climatological feature of this region, the upper-level flow during the flights gave support to the surface high pressure systems that were observed just off the coast of Oregon on 13 and 17 June. These high pressure systems, combined with the relatively low pressures in southern California, give the strong pressure gradients and strong low-level winds observed in the area where the measurements were made. Thus, the conditions observed during these flights may be considered typical for a synoptic pattern where the Pacific high is relatively close to the coast.

3. Description of aircraft data

Aircraft measurements were made to determine the mean and turbulence structure of the boundary layer. Soundings were made to obtain the mean

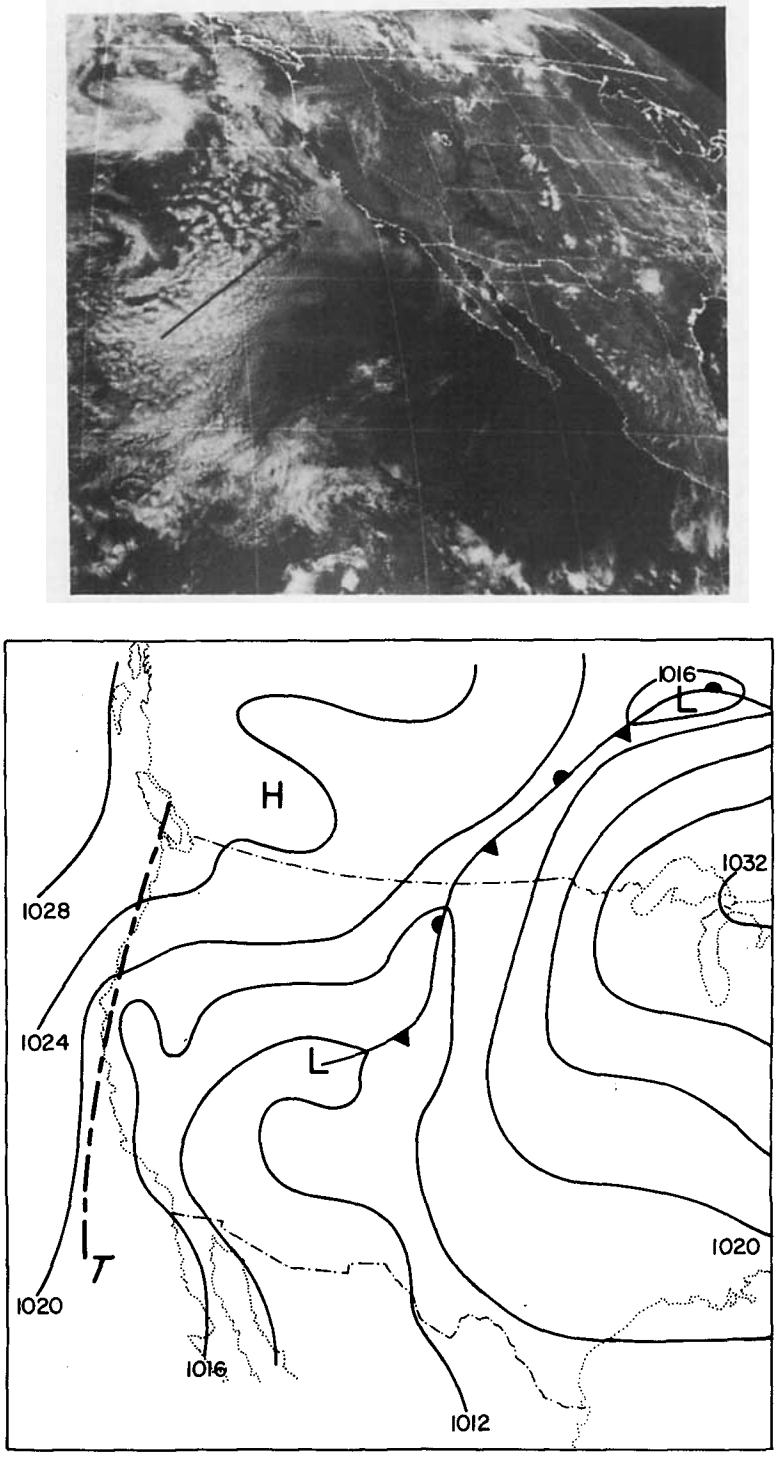

FIG. 1. (upper) GOES-West satellite photograph (1915 GMT) for 5 June 1976. Arrow points to approximate area (indicated by black rectangle) where measurements described in the text were made. (lower) Surface weather map (1200 GMT). Axis of 500 mb trough is shown.

structure, and turbulence data were collected on legs flown at constant pressure levels for a duration of approximately 8–10 min. The mean structure of various quantities was obtained from data recorded at 1 Hz and turbulence quantities were obtained from data recorded at 20 Hz.

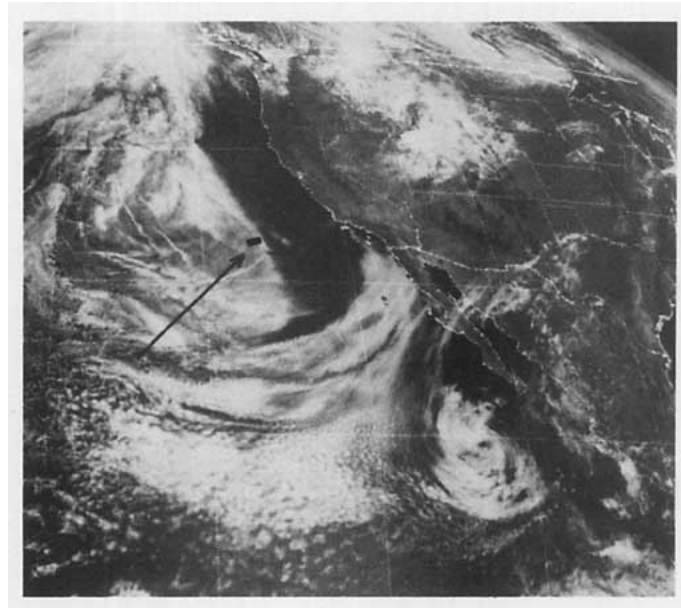

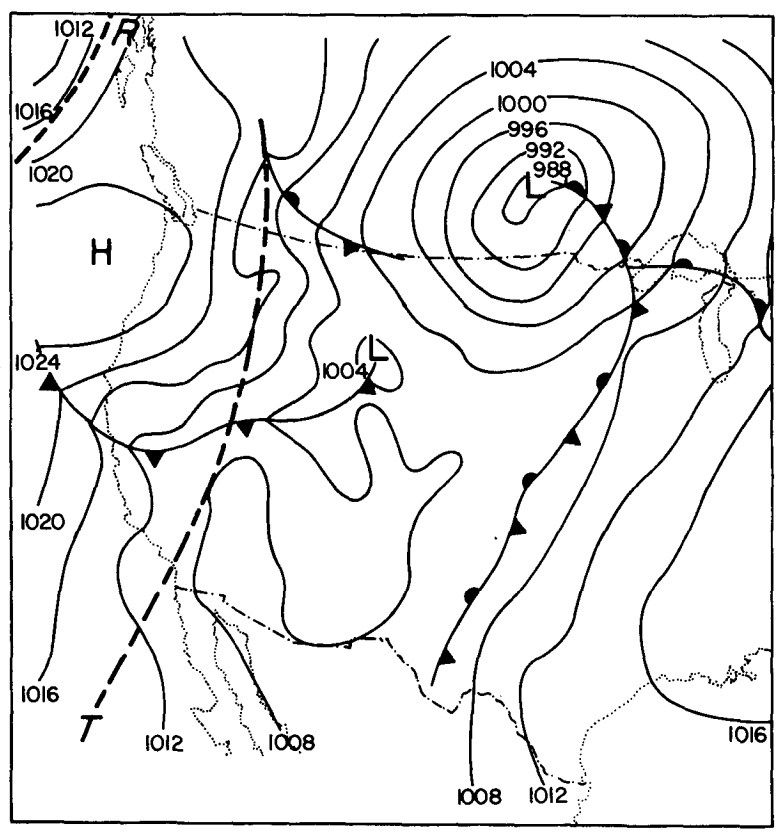

FIG. 2. (upper) As in Fig. 1a but for 1915 GMT 13 June 1976.
(lower) As in Fig. 1b but ridge axis also shown.

A complete description of the instrumentation and data collection on the NCAR Electra for this experiment is given by Wakefield and Schubert (1976) and Brost *et al.* (1982a). A brief description of the instrumentation used for the measurements reported in this paper is given below. Winds were obtained using the gust probe and the inertial navigation system. Brost *et al.* (1982a) found a bias in the slip angle measured by the gust probe. In their study this bias was corrected as a function of true air speed. In this

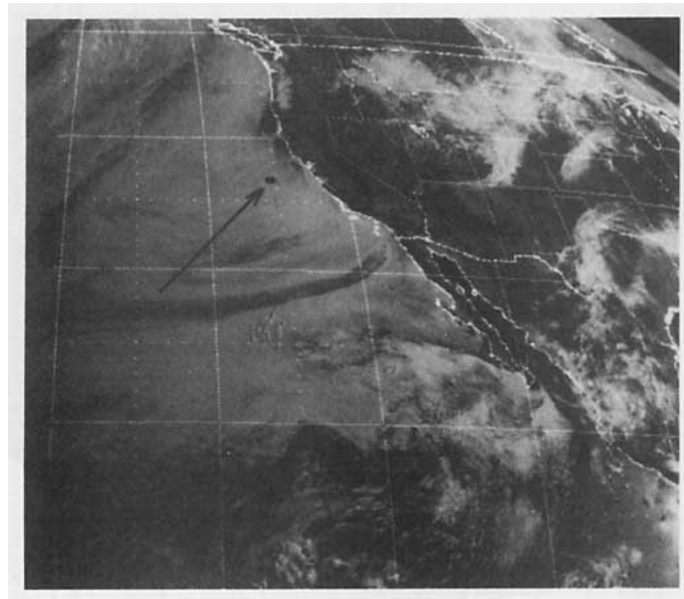

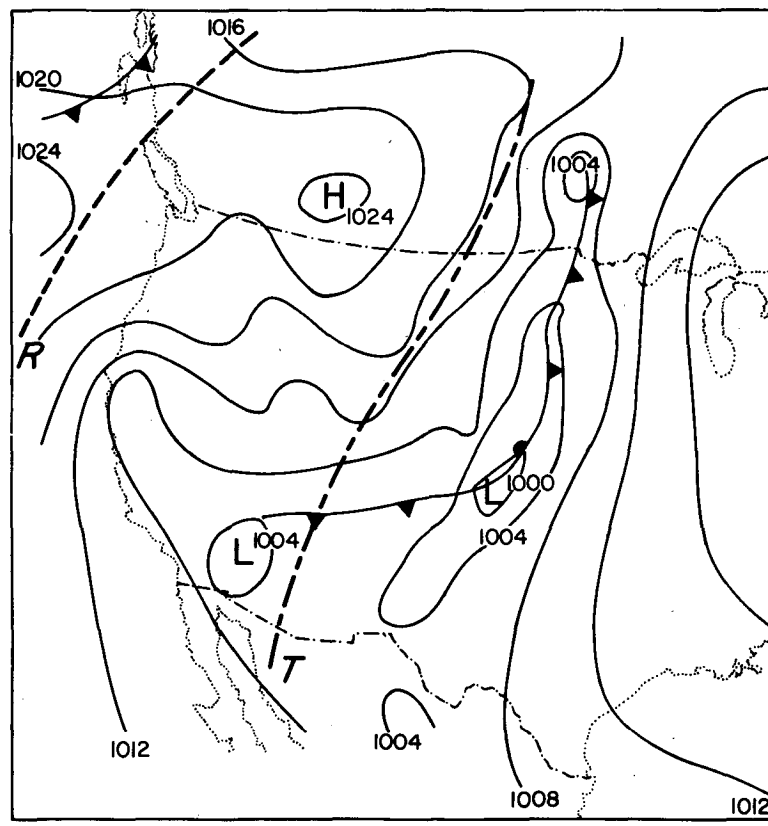

FIG. 3. As in Fig. 2 but 1515 GMT 17 June 1976 satellite photograph.

study uncorrected winds are used, since (as noted in Brost *et al.*) the bias has little effect on the fluctuations in the vertical component of the wind and in the mean horizontal components of the wind.

Air temperature was measured with a number of sensors. A Rosemount sensor was mounted on the nose boom of the aircraft and another was mounted on the fuselage. Both measure total temperature; data from the fuselage sensor was filtered and recorded at a 1 Hz rate while the nose-boom temperature was filtered and then recorded at 20 Hz. Air temperature was obtained from the total temperature using a standard airspeed correction (Lenschow and Pennell, 1974).

Although the housing of the Rosemount is designed to prevent water droplets from impinging on the sensor, under various cloud conditions this sensor can become wet (Lenschow and Pennell, 1974). Albrecht *et al.* (1979) compared temperatures obtained with the fuselage-mounted Rosemount with temperatures obtained with a side-viewing infrared radiometer (manufactured by Barnes Engineering, Model PRT-6). The heat fluxes calculated using 1 Hz values from these sensors and vertical velocity w for an 8.5 min turbulence leg gave values that differed by ~ 5 W m^{-2} (Albrecht *et al.*, 1979). It was suggested that slight wetting of the Rosemount sensor may have been responsible for this difference. A subsequent calculation of the heat flux using 1 Hz temperature values from the nose-boom Rosemount compared favorably with the heat flux from the radiometer temperatures. Unfortunately the radiometer data were contaminated by intermittent noise, prohibiting further in-cloud intercomparisons between the radiometer and Rosemount temperatures.

Further comparisons were made, however, between heat fluxes calculated using 1 Hz data from the nose- and fuselage-mounted Rosemounts. The heat fluxes obtained on the three flights described above for 20 turbulence legs (each of 8–10 min duration) where no liquid water was detected give the average difference between the heat flux calculated with the two Rosemount sensors as 0.3 ± 1.6 W m^{-2}. For 17 in-cloud turbulence legs flown during these flights the nose-mounted sensor gave an average heat flux that was greater than that obtained with the fuselage sensor by 3.7 ± 2.8 W m^{-2}. Although the in-cloud differences may be due to wetting problems, it is not clear why such problems would affect one sensor more than the other. For the results presented here only the nose-mounted Rosemount is used for flux calculations. Overall, the liquid water content of the clouds is sufficiently small that wetting does not appear to be a major problem. However, the in-cloud heat fluxes calculated with the Rosemounts should be viewed with some uncertainty.

Mean values of water vapor content were obtained with a dew-point hygrometer. A Lyman-Alpha hygrometer was used to obtain water vapor content for turbulence quantities. Although the Lyman-Alpha sensor would occasionally give noisy in-cloud results, these periods were easily identified and water vapor measurements from these periods were not analyzed.

Wet-bulb temperatures on in-cloud legs were obtained with a small, lint-covered bead thermistor designed by D. Lenschow. Cloud liquid water kept the sensor wet and it remained wet for several minutes after exiting a cloud. The wet-bulb temperature obtained with this sensor was corrected for the dynamic heating effects described by Lenschow and Pennell (1974). The required recovery factor was calculated in the following two ways: 1) obtaining a linear relationship between raw wet-bulb temperature and airspeed during in-cloud legs and 2) comparing the average wet-bulb temperature obtained with the wet-bulb thermistor to the wet-bulb temperature derived from the mean (Rosemount) air temperature and the water vapor content obtained from the dew-point hygrometer. These two methods gave comparable values for the recovery factor.

As an additional check of the performance of the wet bulb, in-cloud fluxes of equivalent potential temperature ($\overline{w'\theta_e'}$) obtained using the wet-bulb thermistor and those calculated using θ_e from temperature and humidity measurements were compared. The θ_e fluxes obtained with the wet-bulb sensor were found to be consistently less than those obtained with θ_e calculated from temperature T and mixing ratio q and relatively insensitive to the specification of the recovery factor needed to correct for the airspeed. A comparison of the w–θ_e cospectra obtained using the two methods for obtaining θ_e are in good agreement at lower frequencies, but at higher frequencies cospectral estimates obtained using $\theta_e(q, T)$ are greater than those obtained using $\theta_e(T_w)$. These differences appear to be due to the relatively slow response of the wet-bulb sensor.

Cloud liquid water content was obtained using a Forward Scattering Spectrometer Probe (FSSP, manufactured by Particle Measuring Systems) to obtain droplet concentrations in the 2–30 μm diameter range. These data were obtained for 1 s sampling periods. Brost *et al.* (1982a,b) used estimates from a Particle Measurements System Optical Array Probe (OAP) to show that in some cases the contribution of larger droplets to the total water content may be significant. However, these data were not used in this analysis. Further discussion of this point is given in Section 4.

Upward and downward infrared irradiances (3–45 μm wavelengths) were obtained using Eppley pyrgeometers. A correction based on the temperature differences between the viewing dome of the instrument and the housing temperature (Albrecht and Cox, 1977) was applied to these data. The empirical coefficients needed for this correction were obtained for the upward-facing pyrgeometer by minimizing differences between the downward longwave irradiance $L\downarrow$ obtained during an ascending sounding and $L\downarrow$ obtained during a subsequent descending sounding made in the same region of the relatively solid cloud observed on 17 June. A similar procedure was used to obtain the correction factor needed for the downward-facing pyrogeometer, which measures $L\uparrow$. Although the individual corrections for $L\downarrow$ and $L\uparrow$ due to dome-housing temperature differences were sometimes large, these corrections had little effect on the net flux $L_{\mathrm{NET}} = L\uparrow - L\downarrow$, since the dome-housing temperature corrections tend to cancel.

4. Mean structure

Vertical profiles of boundary layer temperature and moisture were obtained for the clouds observed on

5, 13 and 17 June. Profiles obtained during ascents and descents of the aircraft provide a nearly continuous record of the structure. Averages over the 8–10 min turbulence legs flown at several different levels in and above the boundary layers were also used to define mean profiles.

Although two or three sets of turbulence legs were flown on each flight, a number of the sets were obtained in clouds which varied significantly in their structure over the length of the turbulence legs. In some cases the inversion height was also observed to have considerable horizontal variation. In this paper we select the best cloud conditions sampled in an attempt to detect differences between the characteristics of the three clouds. Turbulence legs were also selected from regions when there was little observed variation in the inversion heights. The soundings shown in this section were made in the vicinity of the turbulence profiles shown.

On 5 June (flight 1, the thin cloud case) two sets of turbulence legs separated by a distance of approximately 150 km were flown. Conditions were similar for both sets of legs, but only the first set is described in detail since notes by flight observers indicate slightly better cloud conditions on this leg. Any major differences between the results obtained and these sets will be noted. The approximate time of these measurements was 1930–2040 GMT. On the 13 June flights, three sets of turbulence legs were obtained but two of the sets were made near the boundary between the clear and cloudy regions shown in Fig. 2a. The cloudiness and inversion height varied significantly along these legs (see Brost *et al.*, 1982a, their Fig. 4). The third set of turbulence legs was flown in relatively uniform conditions to the west of the clear area shown in Fig. 2a and is used in the analysis presented here. The approximate time of these measurements was 1630–1740 GMT. This set of turbulence legs was also analyzed in detail by Brost *et al.* (1982a,b) and was labeled the "13–3" set in their paper.

On 17 June (flight 5) two sets of turbulence legs were flown and the inversion height varied significantly along one set of turbulence legs (Brost *et al.*, 1982, Fig. 6). Conditions were relatively uniform along the other set and several turbulence legs were flown in this area. The approximate time of these measurements was 1345–1500 GMT. Brost *et al.* (1982a,b) also analyzed this set of turbulence legs in detail and referred to it as "17–2."

The thermodynamic structure for the thin cloud case (5 June) is shown in Fig. 4. There is good agreement between the sounding and the leg means. Potential temperature θ is well mixed below cloud base. The bottom part of the 200 m thick cloud layer has a moist adiabatic lapse rate, and in the upper 50 m of the layer the lapse rate is less than moist adiabatic. Other profiles obtained during this flight show a similar structure. An inversion with a potential temperature increase of ~5°C caps the boundary layer at a height of ~950 m.

Intrusions of air that are potentially warmer than the boundary layer are clearly evident in the upper part of the cloud layer. This may be either air entrained into the boundary layer or a sampling of above-inversion air as the aircraft flies in and out of the top of the boundary layer, since both vertical and horizontal variations are sampled in the profile mode.

The water vapor mixing ratio q_v for the thin cloud case decreases slightly with height below the cloud, which is similar to the decrease in height that is observed for dry mixed layers. In the lower part of the cloud layer the mixing ratio has the same decrease with height as the saturation mixing ratio along a moist adiabat. The boundary layer is fairly dry (~6

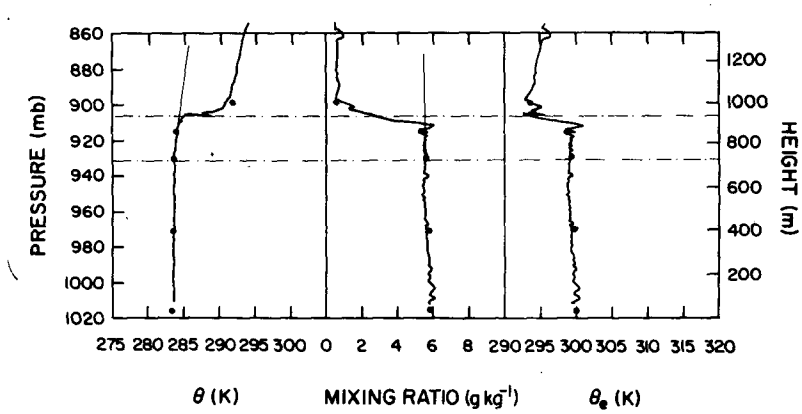

FIG. 4. Profiles of potential temperature θ, mixing ratio q_v and equivalent potential temperature θ_e for thin cloud case (1924–1931 GMT 5 June 1976). Data points are turbulence leg averages. Thin lines indicate approximate position of cloud top and base. Moist adiabatic distributions of θ and q_v are indicated in the cloud layer. Sea surface temperature (from downward-facing radiometer) is 13.9°C.

g kg^{-1}) and the air above the inversion is very dry. The apparent displacement between the height of the inversion and the height of the moisture discontinuity is due to the relatively slow response of the dew-point hygrometer. This profile was obtained during descent.

The combined temperature and moisture jump at the inversion result in a negative jump in equivalent potential temperature θ_e of $\sim$7 K. Since the liquid water content of this cloud is relatively small and has little impact on the virtual effects associated with cloud-top entrainment instability discussed by Randall (1980b) and Deardorff (1980a), this case clearly satisfies the conditions for cloud-top entrainment instability. This point will be discussed further in Section 8.

The horizontal wind components for the thin cloud case (Fig. 5, profile only) show fairly well mixed conditions below the inversion with some shear at the inversion. The winds are from the north-northwest with a magnitude of $\sim$6 m s^{-1} in the mixed layer.

The thermodynamic structure of the broken cloud case (13 June) is shown in Fig. 6. The cloud layer in this case extends from $\sim$200 to 600 m. Cloud base, however, was observed to have significant variation. In the cloud layer, temperature and mixing ratio vary at the same rate as the moist adiabatic values. The relative humidity calculated from the mean leg averages of temperature and water vapor is 97% and varies little throughout the depth of the layer.

The inversion structure for this case is more complicated than the other two cases. Stable layers are located at approximately 600 and 700 m. There is no moisture discontinuity at the lower inversion, but there is a noticeable decrease in moisture at the upper inversion. Clouds were not, however, penetrating to the upper inversion, indicating that this may have marked the top of the boundary layer earlier in the day. The cloud liquid water content was measured to be at a maximum at 400 m and relatively few clouds reached the 600 m inversion. The boundary layer for this case may be in some type of transitional state, although the jump in θ_e at the inversion indicates that this transition is not associated with entrainment instability ($\Delta\theta_e \approx +2.5$ K).

The winds for the broken cloud case (Fig. 7) are relatively strong from the north ($\sim$15 m s^{-1}). Although the u and v components are fairly well mixed in the boundary layer, the shear occurs over a layer of finite depth just below the level of the lowest inversion.

The thermodynamic structure for the solid cloud case (Fig. 8) shows a strong inversion at 600 m and cloud base at $\sim$250 m. As in the thin and broken cloud cases, potential temperature is well mixed in the subcloud layer, and the mixing ratio decreases slightly with height. Unlike the other two cases, the cloud layer is conditionally unstable, since the lapse rate is greater than that of the moist adiabatic. This instability is shown in both the sounding profile and the leg averages and indicates that there may be vertical mixing by moist thermal convection. In this case, as well as in the thin cloud case, the layer becomes more stable just below the very large increase in stability at the inversion. Conditions for cloud-top entrainment instability are not met ($\Delta\theta_e \approx +8$ K).

The solid cloud case clearly has the highest temperatures above the inversion of any of the three cases studied and the temperature above the inversion for the thin cloud case is noticeably less than those for the 13 and 17 June cases. The variations in the above-inversion temperatures of the three cases shown are consistent with the upper-level trough positions shown in Figs. 1, 2 and 3. The 500 mb temperatures in the region where the measurements were made are 5–10°C less on 5 June 1976, consistent with the upper-level trough being located in the region of interest. Since the lowest levels of the boundary layer have temperatures that are close to the surface temperatures and since the vertical structure of the boundary layer is constrained to be approximately dry adiabatic in the subcloud layer and moist adiabatic in the cloud layer, above-inversion conditions strongly control the inversion strength for these three cases.

The winds for the solid cloud case (Fig. 9) show very strong (>20 m s^{-1}) northerly flow in the boundary layer with strong shear at the inversion. Brost *et al.* (1982b) showed the importance of this shear for the turbulence kinetic energy of the boundary layer for this case.

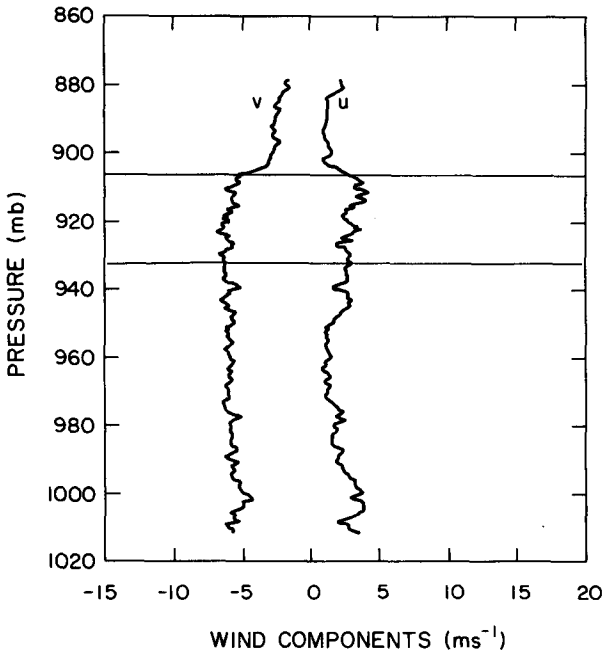

FIG. 5. Profiles of zonal u and meridional v wind components for the thin cloud case.

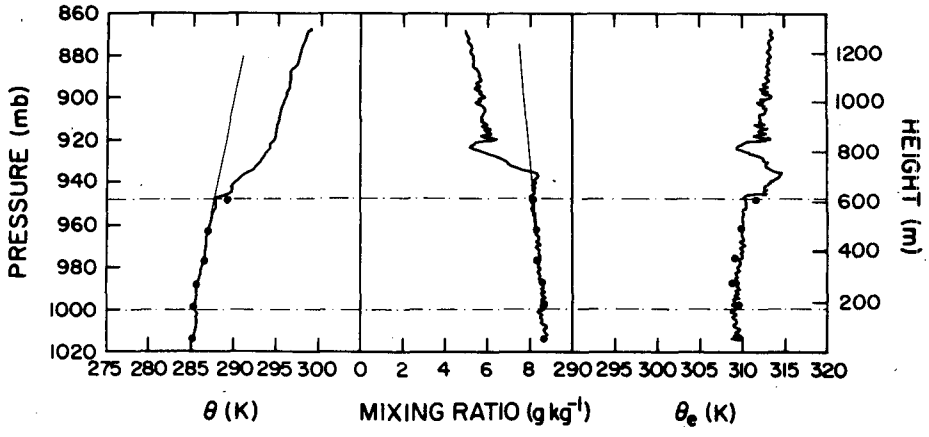

FIG. 6. As in Fig. 4, except for broken cloud case (1744–1749 GMT 13 June 1976). Radiometer sea surface temperature is 14.2°C.

5. Cloud liquid water

Cloud liquid water was obtained with the FSSP by summing the contribution of droplets in 15 size ranges between 2 and 30 μm diameter. Unfortunately, on the 17 June (solid cloud) flight the instrument malfunctioned and only allowed for unambiguous droplet concentrations in four size intervals. Consequently, estimates of cloud water are questionable on this flight, and only averages for the 8–10 min turbulence legs are presented for this flight. There is also, as discussed during a recent workshop (Baumgardner and Dye, 1983), some uncertainty in the liquid water content from properly operating FSSPs due to uncertainties in the sampling volume of the instrument and sizing errors.

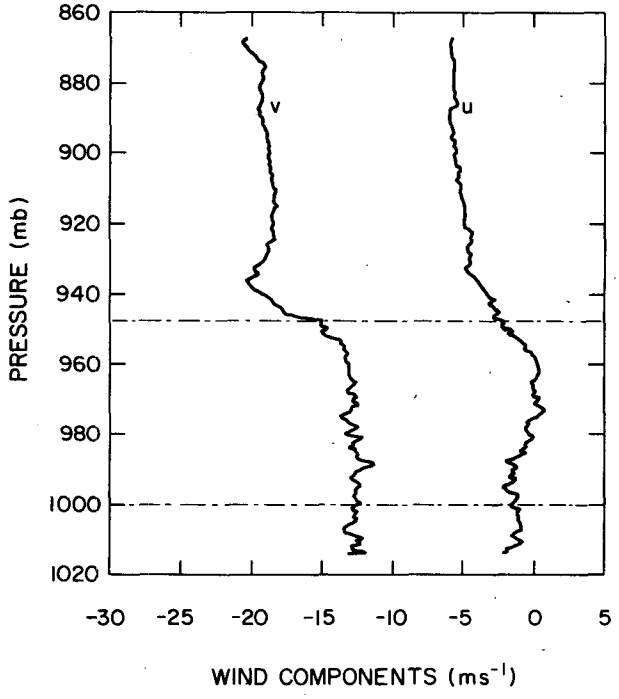

FIG. 7. As in Fig. 5, except for broken cloud case.

The cloud water content obtained from turbulence leg averages using the FSSP is shown as a function of distance above cloud base for the three cloud cases in Fig. 10. The *average* cloud liquid water is relatively small and does not exceed 0.1 g m^{-3} for any of the cases. For the thin cloud case the relatively low liquid water content is due in part to the aircraft sampling at a constant pressure level but cloud-top height and cloud thickness vary horizontally. On the thick broken cloud case, drizzle was observed and may be an important contribution to the total liquid water content (Brost *et al.*, 1982a). In the results here only droplets with diameters between 2–30 μm are included in the liquid water estimates since there may be considerable uncertainty in the drizzle estimates from the OAP (Baumgardner and Dye, 1983). In addition, there is considerable uncertainty in the liquid water for the solid (17 June) cloud case because of the instrument malfunction.

The ratio of the liquid water content from the turbulence leg averages to the adiabatic value is shown in Fig. 11. The vertical coordinate used for this presentation is scaled to the cloud depth and has a value of zero at cloud base and unity at cloud top. The ratios at cloud base have little significance since the adiabatic value is very sensitive to the specification of cloud base. All the measurements show a distinct decrease in the ratio of the total observed cloud water to the adiabatic value in the top part of the cloud layer.

Although the turbulence leg averages give liquid water contents that are significantly less than the adiabatic values, the liquid water content measured during the ascent and descent profiles show peak

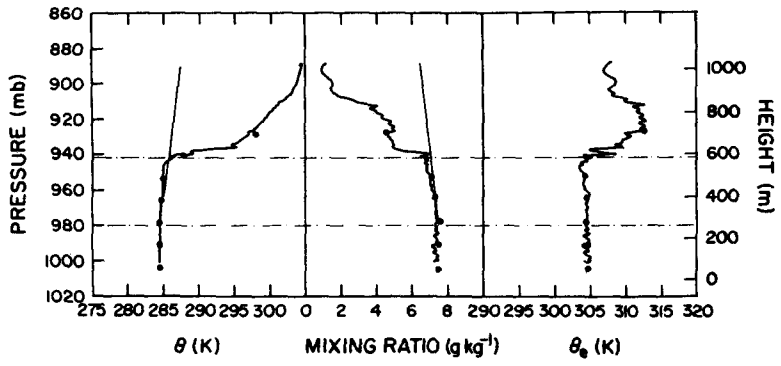

FIG. 8. As in Fig. 4, except for solid cloud case (1315–1319 GMT 17 June 1976). Radiometer sea surface temperature is 9.9°C.

values near cloud base that are much closer to the adiabatic values. In Fig. 12 the envelope of the peak values for the thin cloud and the broken cloud cases are shown. In both cases the peak values of liquid water content in the bottom part of the cloud layer are close to the adiabatic values. The peak values near cloud top, however, are less than the adiabatic values, and for the broken cloud case they are significantly less. In this case, the less-than-adiabatic values may be due to entrainment processes and the formation of drizzle-size droplets that fall to lower levels.

Some of the differences between the cloud structures observed on the three flights may be due to the microphysical properties of the clouds. Average cloud-droplet spectra for turbulence legs at the levels of maximum liquid water content for the three cloud cases are shown in Fig. 13. Here concentrations in only four intervals are shown so that the measurements in the solid cloud case (where the FSSP malfunction reduced the resolution) can be compared unambiguously to the other two clouds. The droplet spectrum for the broken cloud case differs significantly from the other two cases. It has a relatively broad spectrum, which is consistent with the formation of drizzle. For the thin and solid clouds the droplet spectra are relatively narrow, with the maxima occurring at smaller droplet sizes than for the broken cloud. A more detailed description of the droplet distribution for the broken cloud case is given below.

Droplet concentrations for the three cases are given in Table 1 and show that the broken cloud case has

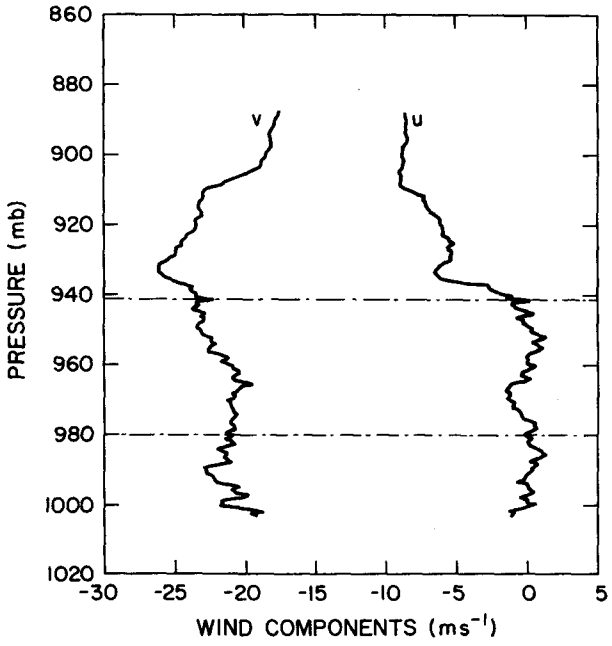

FIG. 9. As in Fig. 5, except for solid cloud case.

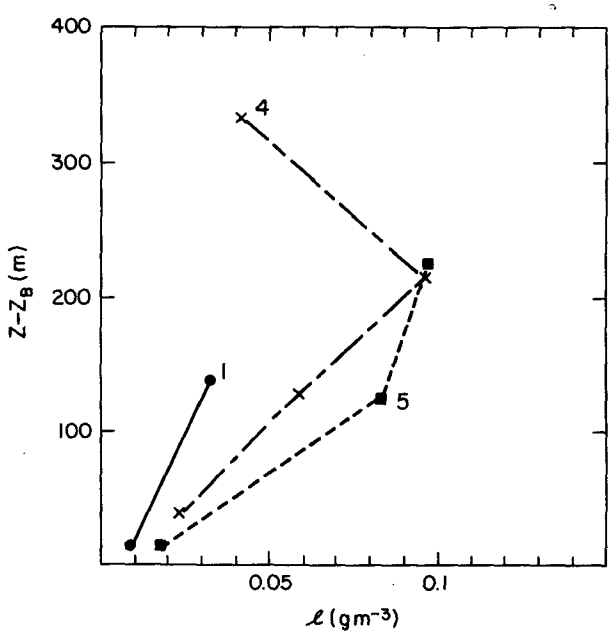

FIG. 10. Liquid water contents for the three cloud cases as a function of distance above cloud base. (Flight 1 = thin case, 4 = broken, 5 = solid).

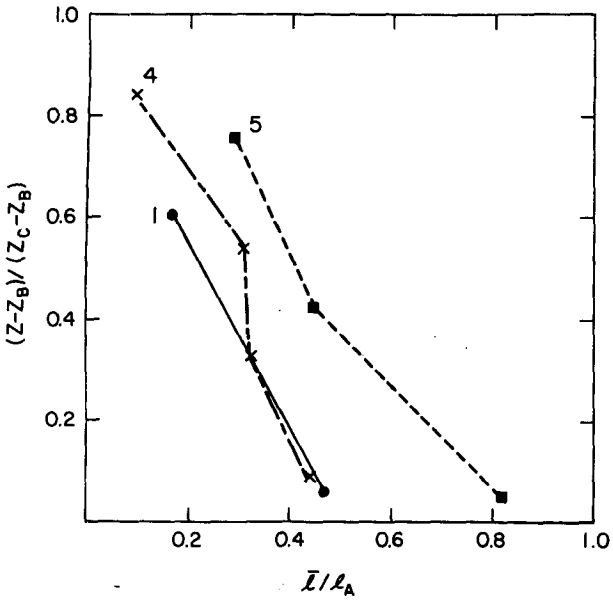

FIG. 11. Ratio of the observed liquid water content from turbulence leg means to adiabatic values. The vertical coordinate is scaled by the cloud depth where z_B is cloud base height and z_c is cloud-top height. (Flight 1 = thin case, 4 = broken and 5 = solid).

about one-fourth of the droplet concentration observed in the solid cloud case. The low concentration of cloud droplets, the broad droplet spectrum and the drizzle observed for the broken cloud case indicate that there may be fewer cloud condensation nuclei (CCN) present than for the other two cases. A relatively low concentration of cloud condensation nuclei is also consistent with the cloud structure shown by the satellite photograph of this region (Fig. 2). The cloud area to the west of the location of the aircraft measurements has a rather tenuous appearance with very clear evidence of cloud trails associated with condensation nuclei emitted by ships in this region. In the cloud trails one would expect a narrower droplet distribution, less drizzle and an enhancement of the cloud. The implication of these results is that cloud structure may in some cases depend on cloud microphysical characteristics. The differences in droplet spectra for the different clouds are qualitatively consistent with the measurements in marine clouds made by Noonkester (1984). He found that differences in the spectra were caused by differences in air masses. The droplet spectra he obtained in continental air masses were narrower and the number of droplets greater than those obtained in marine air masses.

In the 13 June (broken cloud) case four in-cloud turbulence legs were flown. This permitted a detailed examination of the vertical variation of the droplet spectra (Fig. 14). Although the maxima in the droplet concentration clearly increases from a diameter of ~11 μm at cloud base to ~19 μm at cloud top (a distance of ~300 m), the corresponding liquid water content (Fig. 15) has a well-defined maximum at 18 μm and clearly shows that most of the water is concentrated over a relatively narrow range of droplet sizes.

The less-than-adiabatic liquid water content for the leg averages of the clouds discussed above may be due to the turbulent and horizontally inhomogeneous nature of these clouds. For the broken cloud case it was possible to calculate cloud liquid water fluxes from droplet concentrations in 15 size ranges of the FSSP. For these estimates, liquid water concentrations in each size range ℓ_i and vertical velocity w, collected

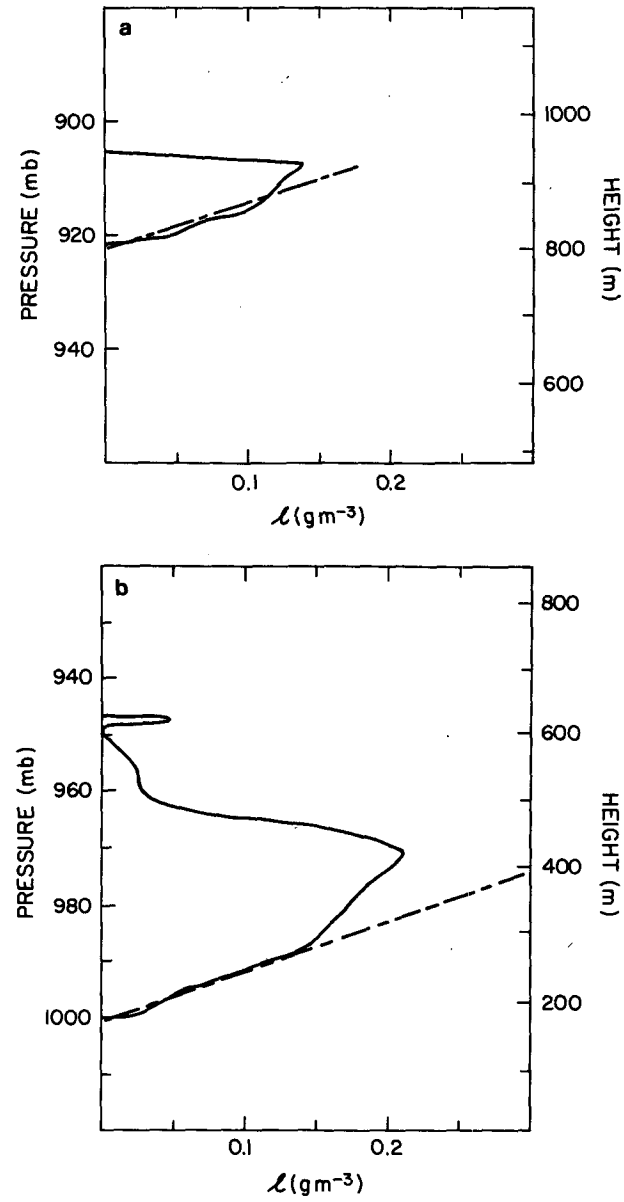

FIG. 12. Envelope of the observed maxima in liquid water content compared with the adiabatic value (broken line) for the (a) thin and (b) broken cloud cases.

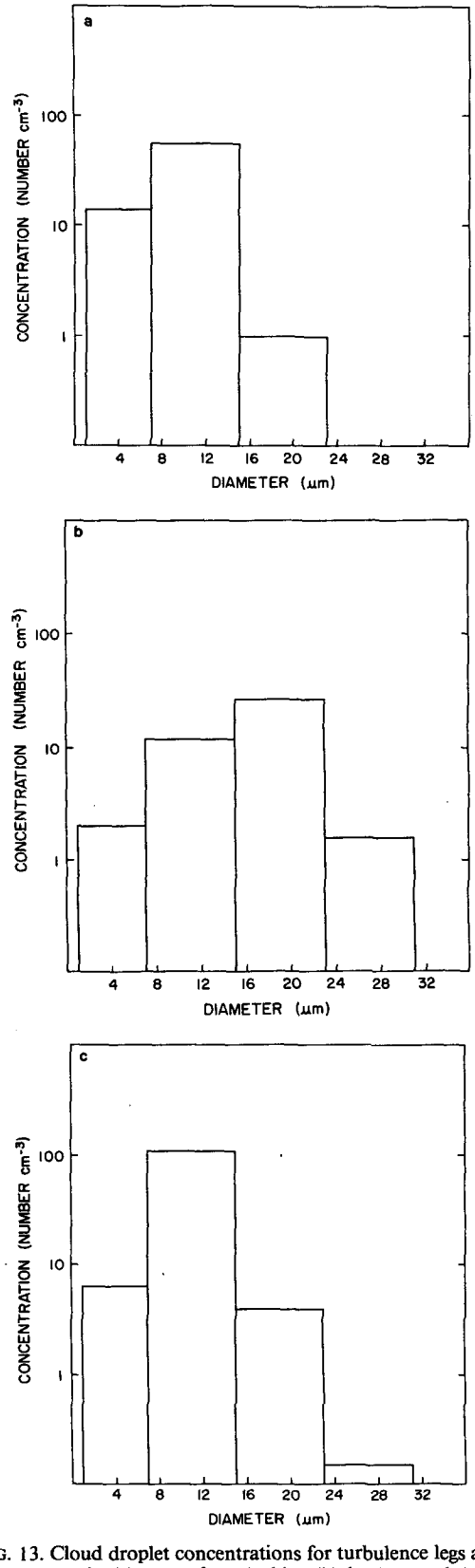

FIG. 13. Cloud droplet concentrations for turbulence legs at level of maximum liquid water for (a) thin, (b) broken and (c) solid cloud cases.

TABLE 1. Concentrations of 2–30 μm diameter droplets.

Cloud	Pressure (mb)	Concentration (No./cm³)
Thin	929.6	46
	915.5	68
Broken	998.9	18
	987.9	32
	977.3	43
	962.9	13
Solid	977.8	52
	964.3	125
	952.6	122

on each turbulence leg (~10 min duration), were divided into three segments of equal length. The mean and linear trend for each of these segments was removed. The deviations from the mean ℓ'_i and w' were then used to calculate the flux $\overline{w'\ell'_i}$ where the overbar is an average over the length of each segment. The estimates of the fluxes from the three segments were then averaged to obtain the flux at a given level. Splitting the turbulence legs into these shorter segments removes contributions to the fluxes due to circulation on scales greater than ~20 km.

The liquid water flux for the 13 June flight is shown in Fig. 16. The flux is dominated by the positive flux for droplets in the range of 12–22 μm; it resembles the liquid water concentration, although the maximum flux occurs at a slightly smaller diameter than the liquid water concentration. Clearly the liquid water content of the updrafts for droplets at 16 μm is greater than that of the downdrafts. For droplets greater than ~26 μm the flux tends to be negative, indicating that the downdrafts have a slightly greater concentration of large droplets than the corresponding updrafts at a given level.

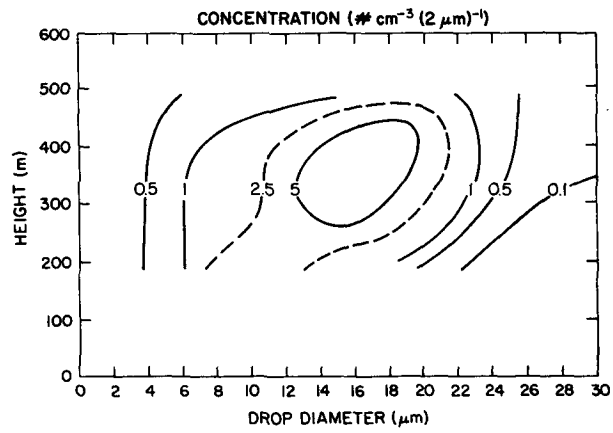

FIG. 14. Cloud droplet concentrations as a function of height for the broken cloud case (13 June).

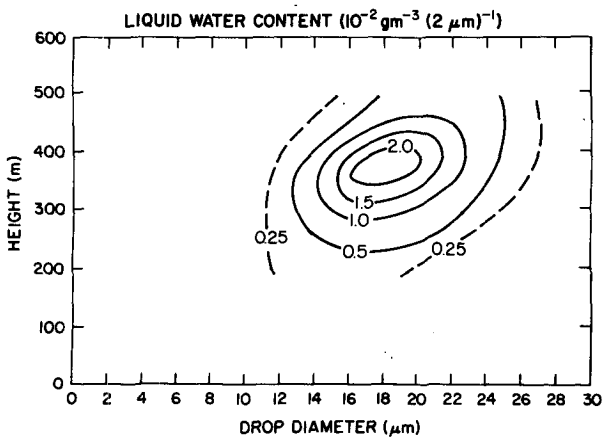

FIG. 15. As in Fig. 14, but for cloud liquid water.

6. Infrared fluxes

Cloud-top radiative cooling is an important component of the simple cloud-topped mixed layer models. Although Lilly (1968) included all of the cooling in the inversion layer, there is some debate about whether all or a portion of some of the cooling should occur below the inversion (Kahn and Businger, 1979; Randall, 1980a; Lilly and Schubert, 1980; Deardorff, 1981). Some of the differences in interpretation depend on how the averaging is defined. Deardorff (1981) argues, for example, that the inversion height varies locally and that the cloud top varies with it. If an entrainment zone of finite thickness is defined such that it encompasses most of the variation of the inversion height, the radiative cooling below this zone depends on the thickness of the zone and the depth over which the radiative cooling occurs within the cloud. Deardorff's description assumes that the interface between saturated and unsaturated air occurs at the interface between turbulent boundary-layer air and quiesent air above.

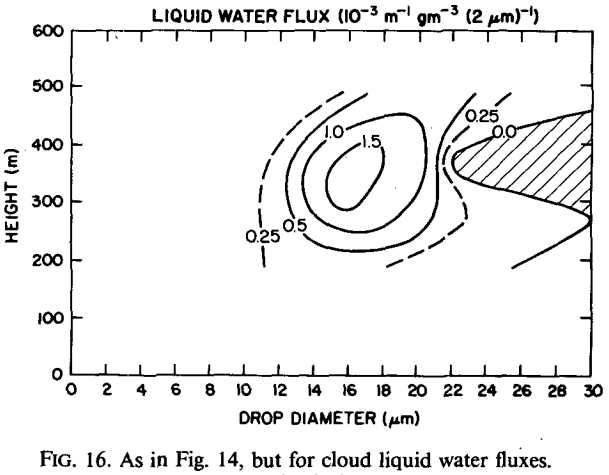

FIG. 16. As in Fig. 14, but for cloud liquid water fluxes. Fluxes are negative in hatched area.

Profiles of net longwave radiation L_{NET} (defined as the upward longwave irradiance $L\uparrow$ minus the downward longwave irradiance $L\downarrow$) corresponding to the thermodynamic profiles shown in Figs. 6 and 8 were obtained from the pyrgeometers during ascents and descents and averages were also obtained for the 8–10 min turbulence legs. During the 5 June flight the upward-facing pyrgeometer, which measures $L\downarrow$, was intermittently noisy due to a faulty connection, and prohibited the calculation of L_{NET} for most of the times of interest. The L_{NET} profiles for the 13 and 17 June clouds are shown in Fig. 17. The cooling is only

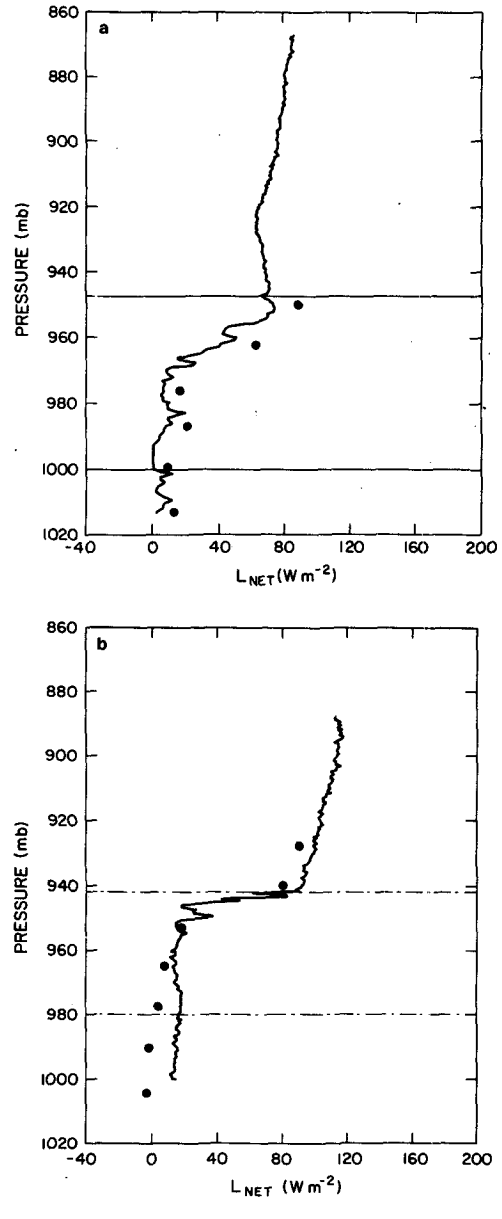

FIG. 17. Net longwave fluxes (L_{NET}) as a function of pressure for (a) broken cloud case and (b) solid cloud case. Data points are the averages for turbulence legs.

approximately proportional to the vertical derivative of these profiles since these profiles also reflect horizontal variations. The profiles obtained from the ascents and descents show vertical distributions similar to the leg-averaged values, although there is a systematic offset. This offset may be due to the instrument not being in complete thermal equilibrium during the ascents and descents.

The cooling for the broken cloud case (Fig. 17a) is distributed over a layer ~ 20 mb thick (~200 m). The increase in the net longwave flux begins at ~970 mb, the level where the liquid water was observed to be a maximum. The temperature and moisture profiles, however, have no sharp gradients at this level. A weak inversion is at ~955 mb—well above the level where the longwave cooling occurs in the cloud layer. There is no doubt that in this case the longwave cooling occurs in the cloud layer, well below the inversion. The relatively broken structure of the cloud near the top of the cloud layer may result in the cooling occurring below the inversion. The net flux near the cloud top for the solid cloud case shows a much sharper transition, although there are clearly fluctuations near cloud top due to horizontal variations in the structure of the cloud.

A further comparison of the structure of the broken and solid clouds is indicated by the standard deviation of $L\downarrow$, calculated for the 10 min turbulence legs (Fig. 18). The pressure is normalized by the pressure at the inversion using the relationship $p^* = (p_s - p)/(p_S - p_I)$ where p_S is surface pressure and p_I is the pressure at the inversion. Clearly in the solid cloud case the downward longwave radiation fluctuates

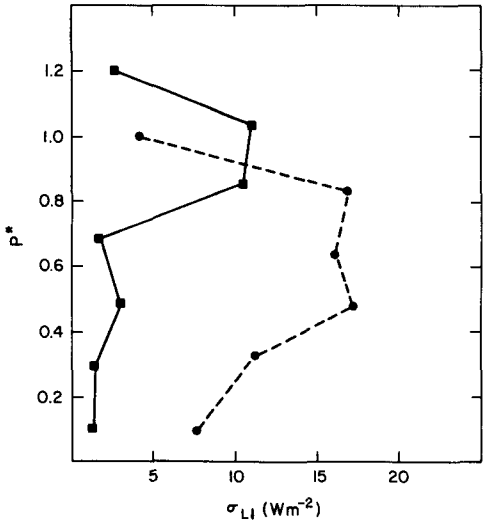

FIG. 18. Standard deviation of downward longwave radiation as a function of $p^* = (p_s - p)/(p_s - p_I)$ where p_s is the surface pressure and p_I is the pressure at the inversion. The solid line is for the 17 June (solid cloud) case and the broken line is for the 13 June (broken cloud) case.

little below cloud base and in the bottom of the cloud layer ($\sigma_{L\downarrow}$ ~ 2 W m^{-2}) and significantly near the inversion. Above the inversion the variability returns to the near-surface values. In the broken cloud case, however, the variation is large in the cloud layer (~15 W m^{-2}), although there is a decrease in the variability near the surface. This decrease is consistent with the fact that the pyrgeometer measures hemispheric radiation. Consequently, even though the cloud is broken, away from the zenith at lower levels the sensor has a view of the sides of clouds; away from the zenith at the top of the cloud, however, the sensor would periodically view clear-sky radiation.

The cloud observed on 17 June was the most solid cloud observed during the experiment. The longwave flux shown in Fig. 17, however, shows evidence of a broken structure near cloud top. To investigate this structure, a detailed analysis was made of the gradients of L_{NET} and the gradient of potential temperature near cloud top. For this analysis the 1 s profile values (Δp ~ 0.3 mb) of L_{NET} and θ were smoothed using a 1-2-1 smoother. These data were then interpolated to standard 0.5 mb levels. Centered finite differences were then used to calculate $\partial L_{\mathrm{NET}}/\partial p$ and $\partial\theta/\partial p$ at 1 mb levels. The quantity $\partial\theta/\partial p$ measures the stability and clearly defines the inversion, and $\partial L_{\mathrm{NET}}/\partial p$ is an indicator of the longwave cooling rate. Values of these quantities near cloud top are shown in Fig. 19. Two profiles are shown: Fig. 19a corresponds to the thermodynamic structure shown in Fig. 3, which was obtained during a descent; Fig. 19b was obtained from an ascent in approximately the same geographical area. The two profiles are shown to determine whether there are any differences that may be due to differences in the time responses of the pyrgeometer and the Rosemount thermometer.

The profiles shown in Fig. 19 clearly show the fluctuations in θ and L_{NET} near cloud top. Since the airspeed of the aircraft is ~100 m s^{-1}, and the ascent or descent for these cases is ~0.40 mb s^{-1}, the change in horizontal distance is 250 m mb^{-1}. The fluctuations at cloud top clearly show horizontal variations in the cloud structure and the height of the inversion. The profiles of $\partial\theta/\partial p$ show that locally there are very large gradients of θ. However, the horizontal variations in the height of this interface show a transition or entrainment zone of ~10 mb (or 100 m) thickness. The variations have an equivalent horizontal scale of ~1 km. The longwave cooling shows variations of approximately the same horizontal scale as the θ fluctuations; however the principal zone of cooling occurs ~50–100 m below the entrainment zone. Unfortunately, in addition to the previously mentioned malfunction of the FSSP, the range of this instrument was set to sample particles with diameters between 0.5 and 7.5 μm during these profiles, which made it impossible to obtain a liquid water profile. It appears, however, that the displace-

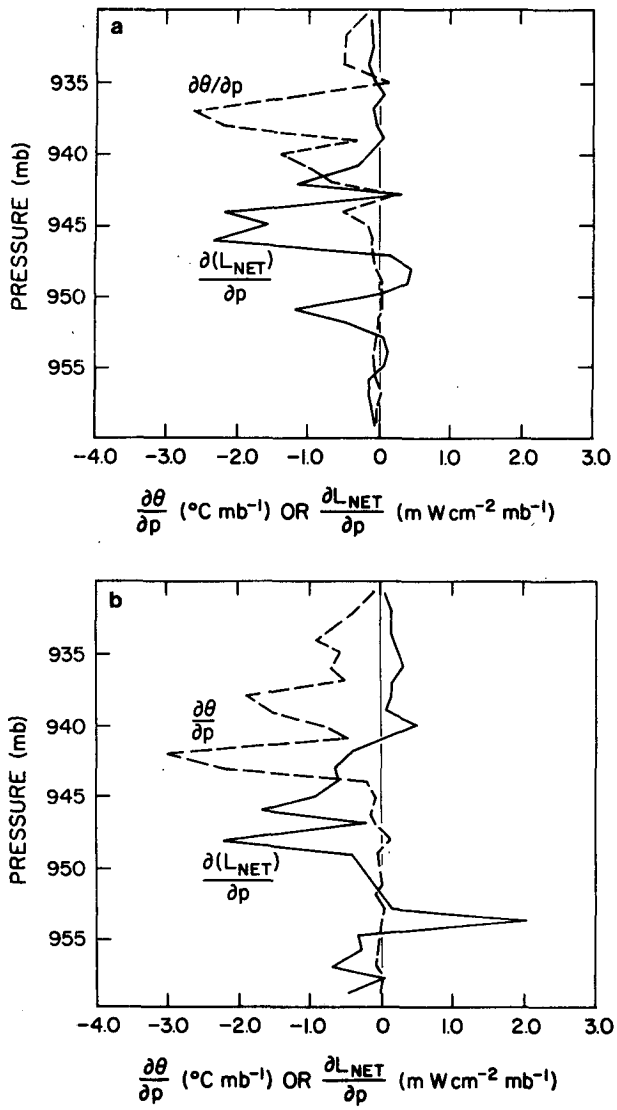

FIG. 19. Profiles at $\partial\theta/\partial p$ and $\partial L_{NET}/\partial p$ for solid cloud case (17 June) for (a) a descent and (b) an ascent in the same area.

ment of the longwave cooling below the transition zone may not be due strictly to the infrared extinction length. Another possibility is that there are variations in the structure of the cloud that clearly occur *below* the inversion layer. These variations, associated with low liquid water content areas or unsaturated regions, may result from the entrainment of air into cloudy regions of the boundary layer. In Section 8 it will be shown that air with thermodynamic properties much closer to mixed layer properties than the above-inversion properties can easily be unsaturated.

A sharp temperature inversion was also observed for the thin cloud case. In this case the FSSP was functioning, and although the upward-facing pyrgeometer had an intermittent noise problem, the data appear to be noise-free during portions of the descent profile shown in Fig. 4. The liquid water content, $\partial\theta/\partial p$ and $\partial L_{NET}/\partial p$ are shown in Fig. 20. As in the solid cloud, the transition zone for temperature and for the net longwave cooling are separated by ~50 m. The horizontal variations that give rise to the structure, however, appear to have a horizontal scale of ~600 m, slightly less than the scale inferred from temperature fluctuations near cloud top for the solid cloud case.

A transition zone in this case also appears in the liquid water content and is located between ~910 and 905 mb, approximately midway between the temperature transition zone and the radiative cooling zone. This structure is consistent with the maximum radiative cooling occurring some distance within the cloud and also with unsaturated areas, or areas with low liquid water content occurring below the inversion. Clearly the liquid water minimum at 909 mb occurs below the temperature transition zone. The air in this region has thermodynamic properties that are more similar to those of mixed-layer air than to those of the above-inversion air.

The potential temperature profiles shown in Figs. 4 and 8 for the thin and solid cloud cases also show a region near cloud top where the sounding gradually becomes more stable. This region, however, is clearly below the region where the sharp transition occurs at the inversion and may correspond to the liquid water transition zone.

What all three cloud cases show is that the cloud structure near cloud top is very important in determining the distribution of radiative cooling. Furthermore, the liquid water structure at cloud top may reflect, but does not necessarily strictly follow, horizontal variations in the inversion height. Thus, the liquid water transition zone may occur below the temperature transition zone associated with the inversion.

7. Heat and moisture fluxes

Heat and moisture fluxes were calculated for the three cloud cases described above using 20 Hz data. The procedure for calculating these fluxes is the same as that described previously for the liquid water fluxes. Data from a turbulence leg are divided into three segments and the mean and linear trend is removed from each of these segments. These are then used to calculate the fluxes for each segment and the average of the three segments is used to obtain the flux at a given level. This filtering process removes contributions to the fluxes due to circulations with horizontal scales greater than ~20 km. Brost *et al.* (1982b) also calculated fluxes for the 13 and 17 June cases, although they eliminated contributions to the fluxes due to circulations greater than 5 km.

Potential temperature fluxes were calculated using 20 Hz Rosemount temperatures, and water vapor

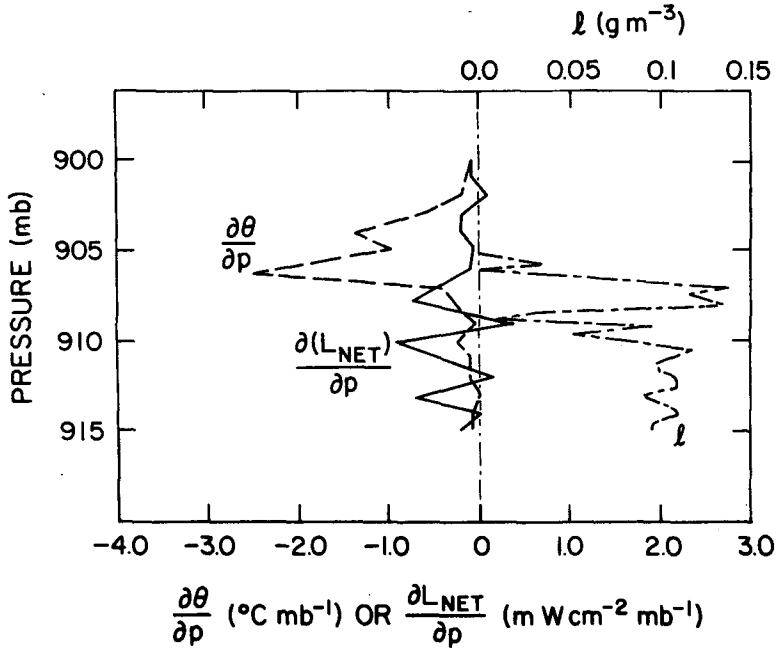

FIG. 20. Profiles of cloud liquid water content, $\partial\theta/\partial p$ and $\partial L_{NET}/\partial p$ near cloud top for the thin cloud (13 June) case.

fluxes were obtained from the Lyman-Alpha water vapor data. Equivalent potential temperature fluxes were obtained using potential temperature deviations θ' and water vapor fluctuations q'_v to obtain θ_e fluctuations using the approximate expression

$$\theta'_e = \theta' + \frac{L}{c_p} q'_v. \tag{1}$$

Equivalent potential temperature fluxes were also calculated directly from the wet-bulb temperature T_w for the in-cloud legs of the solid and broken clouds by assuming $\theta_e(T, q_v, p) = \theta_{es}(T_w, p)$ where θ_{es} is the saturation equivalent potential temperature. On the 17 June flight the in-cloud Lyman-Alpha data were contaminated by high-frequency noise. In this case θ'_e from the wet bulb and θ' from the Rosemount were used with (1) to obtain q'_v.

The potential temperature fluxes for the three cases are shown in Fig. 21. The heat fluxes for the thin and broken cloud cases have a positive heat flux near the surface. Both cases also show a tendency for the heat flux to be slightly positive in the cloud layer but negative in the top part of the cloud layer. For the solid cloud case, however, there is a positive heat flux in the cloud layer with a small, negative heat flux at the surface.

The moisture flux profiles for the three cases are shown in Fig. 22. Although the mean thermodynamic conditions for the thin cloud case satisfy the cloud-top entrainment instability criteria, the turbulence fluxes are clearly moistening the boundary layer and the moisture flux at the inversion is relatively small. The boundary layer is relatively dry in this case, which results in a relatively large surface moisture flux; therefore, the flux convergence for this case would cause the boundary layer to either moisten with time or help balance any local drying due to large-scale horizontal advection that may be contributing to the observed relatively dry boundary layer. The turbulence legs made to the south of these turbulence legs indicated more entrainment (larger moisture flux at the inversion) than the case presented, but these fluxes still tend to moisten the boundary layer slightly. Penc (1983) obtained updraft and downdraft characteristics for the three cloud cases and found no direct evidence (no enhanced updraft or downdraft circulations) for cloud-top entrainment instability for the thin cloud case, although it is possible that it played a role in deepening and drying the layer prior to the time of the measurements.

The moisture fluxes for the broken cloud case (Fig. 22b) would tend to dry the bottom part of the boundary layer and moisten the top part. The cloud liquid water flux ($\rho L\overline{w'q'_\ell}$) is also shown and is about half the magnitude of the water vapor fluxes. The net effect of these fluxes is to dry the bottom part of the cloud layer and moisten the top part. Brost *et al.* (1982b) calculate the drizzle flux using the Optical Array Probe (OAP) to estimate droplet concentrations in the 20–300 μm diameter range. From these concentrations the drizzle flux was calculated and found

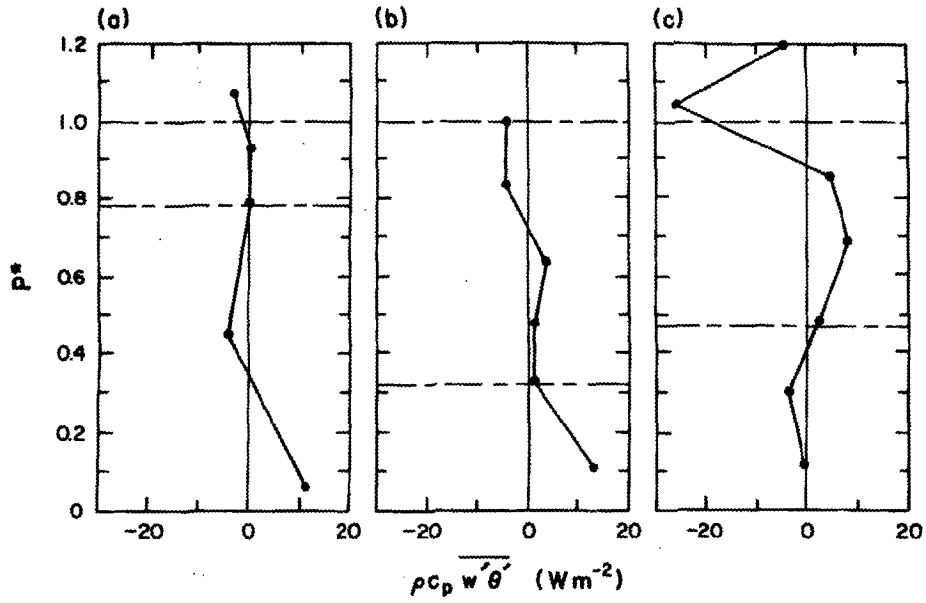

FIG. 21. Potential temperature fluxes for (a) thin, (b) broken and (c) solid cloud cases.

to be very large compared to the cloud liquid water and water vapor fluxes. However, there may be considerable uncertainty in these results since OAP estimates of concentrations are particularly poor in the small diameter range where most of the drizzle droplets were observed. For bigger droplets only a few can have a significant effect on the liquid water content, since the sampling volume is relatively small. Qualitatively, however, the presence of drizzle is consistent with the water vapor and cloud water fluxes shown in Fig. 22b since it tends to moisten the lower part of the boundary layer and dry the top part of the cloud layer where the vapor and water fluxes tend to moisten. In the solid cloud case the moisture fluxes show little moistening or drying of the boundary layer. The large moisture flux peak just above the inversion may be due to sampling in the inversion layer.

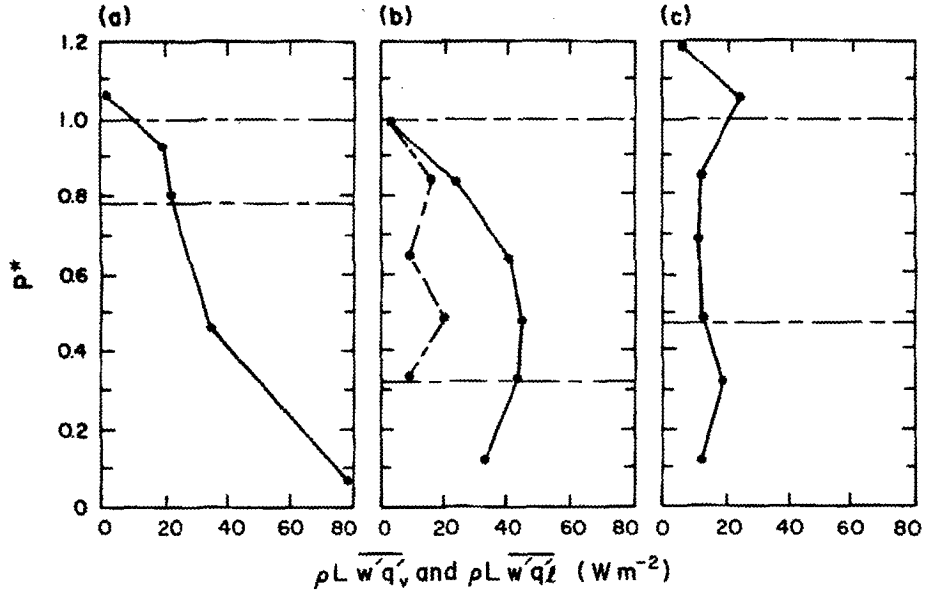

FIG. 22. As in Fig. 20, for water vapor. In-cloud fluxes for solid cloud case were obtained from wet-bulb sensor. The liquid water flux (broken line) is shown for the broken cloud case.

The fluxes of θ_e are shown in Fig. 23 and resemble the water vapor fluxes since they tend to be the dominant term in (1). Overall, these fluxes tend to have a relatively linear variation with height, which is consistent with the flux profile assumed in the simple mixed-layer models. The equivalent potential temperature fluxes show further evidence that the thin cloud case is not in equilibrium or is influenced by advection. The flux convergence in this case would warm the boundary layer at a rate of $\sim 1°C\ day^{-1}$ and moisten it at a rate of $\sim 2\ g\ kg^{-1}\ day^{-1}$.

The equivalent potential temperature flux for the broken cloud case is approximately constant in the lower part of the boundary layer, although the potential temperature and water vapor fluxes vary with height. This is consistent with the drizzle fluxes since they can affect temperature and moisture but do not affect θ_e. In the upper part of the cloud layer the θ_e flux from the wet-bulb sensor has the same divergence as the flux obtained using θ and q_v, but the magnitude differs. For the solid cloud case the profile of the equivalent potential temperature flux does not vary significantly with height.

As concluded by Brost *et al.* (1982b), these results are consistent with the assumptions used in the simple mixed-layer models where the flux of equivalent potential temperature is assumed to have a linear variation with height. The total water flux (vapor and cloud water), however, may not be linear in situations where there is drizzle. In regions where there is radiative cooling distributed in the cloud layer (e.g., the broken cloud case) the assumption that the sum of the radiative flux and the equivalent potential temperature flux is approximately linear (e.g. Deardorff, 1980) is consistent with the results shown for the broken cloud case.

Virtual potential temperature fluxes indicate the generation of turbulence kinetic energy by buoyancy forces. The turbulence kinetic energy budgets calculated by Brost *et al.*, (1982b) for the 13 and 17 June flights included turbulence profiles obtained in cases where there was little cloud or where there was substantial variation in the cloud structure over the distance of the turbulence legs. Because of the strong winds observed on the 13 and 17 June flights, Brost *et al.* (1982b) found that the shear generation was an important component of the turbulence kinetic energy. The liquid water fluxes calculated for the broken cloud case have a relatively small effect on the virtual heat fluxes.

The virtual fluxes for the cases considered in this paper are shown in Fig. 24. The thin and broken cloud cases resemble the virtual temperature fluxes calculated by Deardorff (1980b) using his three-dimensional turbulence model for a simulation over land. In this case the main generation due to buoyancy results from surface forcing with a tendency for the fluxes to be slightly positive in the cloud layer. These fluxes may also be consistent with cold air advection that may be occurring in these regions.

The virtual heat flux profile for the solid cloud case, however, is similar to that obtained for the steady-state mixed-layer models where the surface fluxes are relatively small and negative with buoyancy generation in the cloud layer (Schubert *et al.*, 1979a).

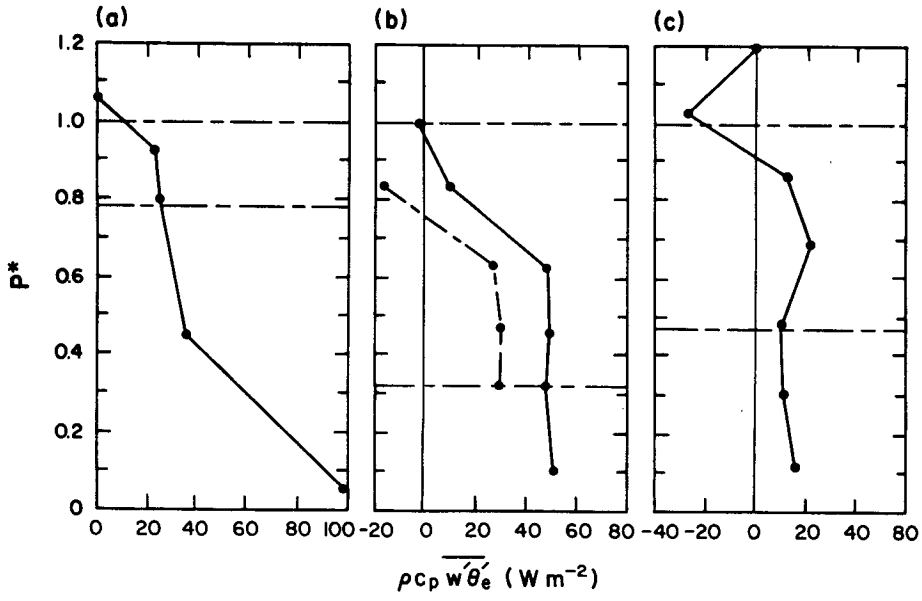

FIG. 23. Equivalent potential temperature fluxes for the three cloud cases. In-cloud fluxes for the solid cloud case are from wet-bulb sensor. In-cloud fluxes for broken cloud case obtained from wet-bulb (broken line) are shown in addition to the fluxes calculated using θ and q_v.

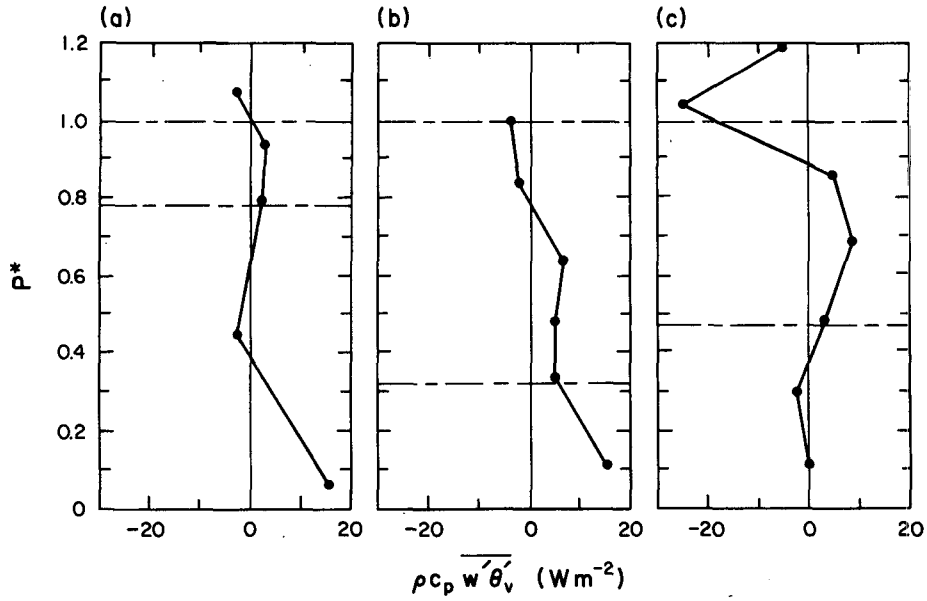

FIG. 24. As in Fig. 21, but for virtual potential temperature fluxes.

8. Cloud-top structure and cloud-top entrainment instability

The analysis of the radiative fluxes and the liquid water indicates that there may be regions just below the inversion that are unsaturated. Thus, the visible cloud top in some regions may not coincide with the inversion height. This may be particularly true in regions where there is entrainment. To illustrate this situation, we consider the mixing of a saturated parcel with an unsaturated parcel and examine the conditions that give an unsaturated mixture. This analysis is also used to determine the conditions where the density of the mixture is greater than that of the initially saturated parcel. These conditions place further constraints on the cloud-top entrainment instability criteria discussed by Randall (1980b) and Deardorff (1980a). Hanson (1984b) gives a comprehensive discussion of cloud-top entrainment instability and some of the physical processes associated with it.

We consider a saturated parcel of mass m_1 with thermodynamic properties θ_1, q_{v1} and $q_{\ell 1}$ and an unsaturated parcel of mass m_2 and thermodynamic properties θ_2 and q_{v2}. After mixing, the resulting parcel has a mass $m_f = m_1 + m_2$ and a thermodynamic state θ_f, q_{vf} and $q_{\ell f}$. It is useful to define $\chi = m_2/m_1$, equivalent potential temperature in approximate form as $\theta_e \approx \theta + Lq_v/c_p$ (Betts, 1973), and $\gamma \equiv L \times (\partial q_v^*/\partial_T)_p/c_p$ where q_v^* is the saturation mixing ratio. In mixing the parcels it is assumed that no radiative or precipitation processes are occurring so that θ_e total water $q = q_v + q_\ell$ are conserved.

The conservation of total water may be written as

$$(m_1 + m_2)(q_{vf} + q_{\ell f}) = m_1(q_{v1} + q_{\ell 1}) + m_2 q_{v2}, \quad (2)$$

which can be rewritten as

$$q_{\ell f} = (q_{v1} - q_{vf}) + q_{\ell 1}\left(\frac{1}{1+\chi}\right) + \Delta q_v\left(\frac{\chi}{1+\chi}\right), \quad (3)$$

where $\Delta q_v = q_{v2} - q_{v1}$. The conservation of equivalent potential temperature can be written as

$$\theta_{ef}(m_1 + m_2) = \theta_{e1}m_1 + \theta_{e2}m_2, \quad (4)$$

or

$$\theta_{ef} = \theta_{e1} + \Delta\theta_e\left(\frac{\chi}{1+\chi}\right), \quad (5)$$

where $\Delta\theta_e = \theta_{e2} - \theta_{e1}$.

If the final parcel is saturated, then $q_{vf} = q_{vf}^*$ and, since the initial parcel is saturated $q_{v1} = q_{v1}^*$. If the changes in temperature associated with the mixing are relatively small,

$$q_{vf} - q_{v1} = \gamma\frac{c_p}{L}(\theta_F - \theta_1) = \frac{c_p}{L}\frac{\gamma}{1+\gamma}(\theta_{ef} - \theta_{e1}). \quad (6)$$

Equation (5) can be combined with (3) and (6) to give

$$q_{\ell f} = \left(\frac{1}{1+\chi}\right)q_{\ell 1} - \frac{c_p}{L}\left(\frac{\gamma}{1+\gamma}\right)\left(\frac{\chi}{1+\chi}\right)\Delta\theta + \left(\frac{1}{1+\gamma}\right)\left(\frac{\chi}{1+\chi}\right)\Delta q. \quad (7)$$

This gives an expression for the liquid water content of the final parcel as a function of the thermodynamic state of the two initial parcels and the ratio of the masses of the two parcels. Since $\chi \geqslant 0$ and $\gamma \geqslant 0$, as the temperature of the unsaturated parcel increases

relative to the saturated parcel ($\Delta\theta$ increasing), the liquid water content of the final mixture will decrease. Likewise, as the water vapor mixing ratio of the unsaturated parcel decreases, the final liquid water would also decrease. For stratocumulus the mixing may be viewed as unsaturated parcels entrained into the boundary layer mixing with saturated boundary-layer parcels. In this case $\Delta\theta > 0$ and $\Delta q < 0$, so that the mixture that results from the mixing of a saturated and unsaturated parcel will have a smaller liquid water content than the initial saturated parcel.

Equation (7) can be applied at the point where $q_{\ell f} = 0$. This defines the saturation point (Betts, 1982). For given thermodynamic conditions the mixture will be saturated if χ is less than

$$\chi_{\text{crit}} = \frac{(1+\gamma)q_{\ell 1}}{\gamma c_p \Delta\theta - L\Delta q_v}. \tag{8}$$

Values of χ_{crit} for various values of $\Delta\theta$ and Δq are shown in Fig. 25. The values shown are for $q_{\ell 1} = 1$ g kg^{-1} and $\gamma = 1.35$, but are easily scaled to any value of $q_{\ell 1}$. In a particular application γ can be calculated using given thermodynamic conditions. Although radiative processes have been ignored, radiative cooling would be equivalent to decreasing $\Delta\theta$ (Betts, 1983) and would increase χ_{crit}.

The $\Delta\theta$ and Δq values corresponding to the jumps at the inversion for the three cloud cases considered above are shown in Fig. 25. For the thin cloud case the maximum liquid water value observed during the descent profile (shown in Fig. 11a) is ~0.12 g kg^{-1}. If this value is assumed to be $q_{\ell 1}$, then $\chi_{\text{crit}} \sim 0.03$. Thus, if an unsaturated parcel of above-inversion air mixes with a saturated parcel of equal mass with boundary-layer thermodynamics, the resulting mixture will be unsaturated. The mixture would only be saturated if the mass of the saturated parcel were 30 times greater than the mass of the unsaturated parcel. Thus, unsaturated regions in the transition zone near the inversion can have thermodynamic characteristics (other than liquid water) that are very close to the characteristics of the saturated air in the boundary layer and quite different from the characteristics of the unsaturated air above the inversion. A small χ_{crit} value also indicates that a finite amount of time is required for the mixing to occur since there is more than an order of magnitude difference in the masses of the two parcels. The actual time will be a function of the magnitude of the masses involved in the mixing. In the entrainment and mixing processes we envision a finite unsaturated parcel of above-inversion air being entrained into the cloud layer and subsequently mixing with increasing amounts of cloud-layer air. Thus the time required for the mixture to obtain χ_{crit} will depend on the mass of unsaturated air entrained and will increase as χ_{crit} decreases.

In the broken cloud case, the inversion is very weak and there is no jump in q at the inversion. Thus, $\chi_{\text{crit}} = 2.15$ (kg g^{-1}) q_{v1}. However, as discussed previously, drizzle in this case tends to deplete cloud water in the upper part of the cloud layer. The maximum value near the inversion (Fig. 11b) is less than 0.05 g kg^{-1}, which corresponds to an χ_{crit} value of ~0.1. For the solid cloud case, direct measurements of the maximum liquid water content are not available. However, using the adiabatic values near cloud top gives $\chi_{\text{crit}} \approx 0.1$.

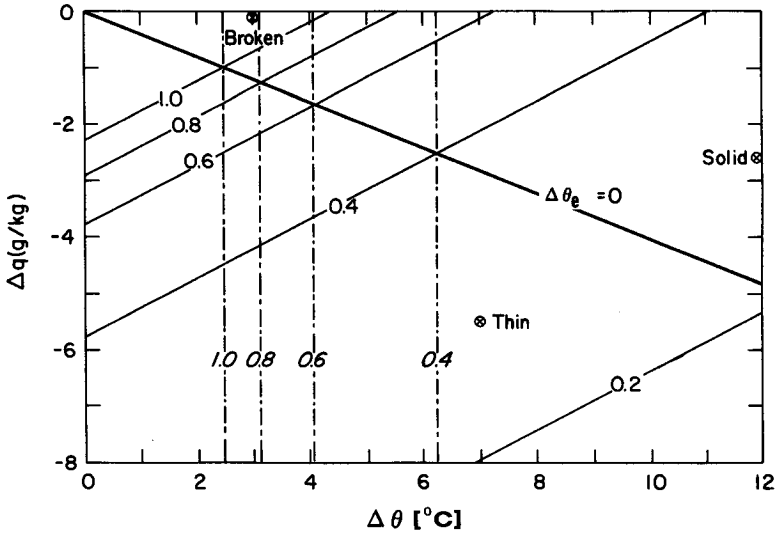

FIG. 25. Critical values of χ or (w_e/w^*) for a mixture to be just saturated (solid) or for an unsaturated mixture to be negatively buoyant with respect to saturated cloud parcels (dashes). These values were obtained for a saturated parcel with an initial liquid water mixing of 1 g kg^{-1}.

Obviously for a given set of conditions the depth of the cloud layer and precipitation processes can affect the cloud liquid water content. This can have a significant effect on χ_{crit} and hence may have an impact on the cloud structure.

Schubert *et al.* (1979a) described the circulation in stratocumulus using a simple updraft–downdraft circulation. Betts (1983) has recently described such a circulation using saturation points. In this formulation it is useful to define the velocity scale for the internal circulation as w^*. For a circulation where the area associated with updrafts is equal to the area associated with downdrafts, the vertical velocities in these two areas are approximately equal. In this simple circulation, the χ value can be shown to be roughly equivalent to the ratio w_e/w^* where w_e is the entrainment velocity at the inversion. For this circulation the updraft–downdraft differences can be written as a function of w_e/w^* and the jumps in θ and q_v at the inversion (Betts, 1978). The critical values of the ratio w_e/w^* can be obtained using (7). In this case, if w_e/w^* exceeds the critical value and if it is assumed that within the updraft and downdraft regions the thermodynamic properties are relatively uniform, the downdraft will be unsaturated. In the Betts (1983) formulation this is simply a statement that the saturation level for the downdraft air is above the inversion. Thus as the entrainment rate increases so does the height of the saturation level of the downdraft and, as pointed out by Deardorff (1980a), the cloud base in the downdraft region becomes higher than the cloud base in the updraft region. Deardorff (1980a) suggested that the breakup could be related to a critical ratio of w_e/w_* by the relationship

$$(w_e/w_*)_{crit} \propto \frac{(q_\ell)_{max}}{-\Delta q_v}, \tag{9}$$

where w_* is the generalized mixed-layer free convective velocity, which should be proportional to the mass flux circulation velocity w^* defined above. Nicholls and LeMone (1980) showed such a proportionality ($w^* \approx 0.3w_*$) for their aircraft study of subcloud layers associated with undisturbed conditions in the tropics.

Clearly, the critical value given by (9) is similar to the critical value given by (8). The critical value given by Deardorff (1980a), however, does not account for the change in the saturation mixing ratio associated with the entrainment of unsaturated warm air and the subsequent cooling due to evaporation.

This analysis has some implications about cloud-top entrainment instability. For the treatment here, virtual effects will be neglected, although as indicated by Randall (1980b) and Deardorff (1980a) these virtual effects should be included. For the situation described previously for the mixing of two parcels, Eqs. (5) and (6) may be used to define the temperature of the final mixture as

$$\theta_f - \theta_1 = \frac{\Delta\theta_e}{1+\gamma}\left(\frac{\chi}{1+\chi}\right), \tag{10}$$

provided the final mixture is saturated.

Thus, if $\Delta\theta_e$ (or equivalently $\Delta\theta_w$ where θ_w is wet-bulb potential temperature) is negative, $\theta_f - \theta_1 < 0$ and the mixture would be negatively buoyant relative to the initial saturated parcel, which is equivalent to what is commonly referred to as "cloud-top entrainment instability" when it applies to a cloud layer. The criterion given by (10), however, is independent of the magnitude of the mass ratio χ, although the magnitude of the temperature difference does depend on χ. A crucial assumption in (10), however, is that the final mixture is saturated. But, as was shown above, for specific values of χ, the mixture may not be saturated and the criteria is no longer given by (10).

For a situation where the final parcel is unsaturated

$$\theta_f - \theta_1 = \Delta\theta\left(\frac{\chi}{1+\chi}\right) - \frac{L}{c_p}\left(\frac{1}{1+\chi}\right)q_{\ell 1}. \tag{11}$$

Although the condition that θ_f be less than θ_1 was satisfied for any χ in Eq. (10), in this case θ_f will be less than θ_1 if $\chi < Lq_{\ell 1}/(c_p\Delta\theta)$. In this case the instability depends on the liquid water content and $\Delta\theta$. Thus, in clouds that have a large liquid water content capped by inversions that are relatively weak, the constraint on χ is significantly reduced. In the clouds described in this study the water content is relatively low and the constraint given by (8) may be an important factor. Hanson (1981) also presents a discussion on entrainment associated with unsaturated air masses.

What is clear from the above discussion is that if $\Delta\theta_e < 0$ (or the appropriate criterion including virtual effects) at the top of the cloud-topped mixed layer, cloud-top entrainment instability may not be met until the resulting mixture is near saturation. Thus if a parcel is entrained into a cloud layer and subsequently mixes with a parcel of equal mass, the resulting mixture would not be negatively buoyant, for typical stratocumulus conditions. Only if the entrained air mass is mixed with a significantly larger cloud mass will the resulting mixture be negatively buoyant. Since such mixing requires a finite amount of time, the entrainment instability would not occur instantaneously as is often assumed. The actual time required for the mixing will depend on the scale of the entrainment process. For entrainment in deeper cumulus clouds, such as that discussed by Squires (1958) and Emanuel (1981), the instability would be realized more easily since the liquid water content in deeper clouds is much larger than in stratocumulus and the inversion at cloud top tends to be weaker. Thus χ_{crit} is larger and more easily obtained.

The process described above may be crucial in the

thin cloud case, where even though the cloud-top entrainment instability is clearly met, the turbulence flux measurements described here and in Penc (1983) give little evidence that the instability is occurring. Since a finite time may be required to realize the instability, it is not clear that the instability will always *directly* increase entrainment at the inversion, although it could affect the mass circulation w^* and thus increase the entrainment rate *indirectly*. A similar argument was made by Stage and Businger (1981b). Since χ_{crit} (or w_e/w^*) is the crucial parameter in determining whether the mixture is saturated, it is possible to have the cloud-top entrainment instability conditions defined by Deardorff (1980a) and Randall (1980b) satisfied without totally breaking up the cloud layer, but only changing the circulation characteristics (updraft and downdraft velocities, cloud base variations, etc.) of the cloud. Another possibility is that cloud-top entrainment instability can dry the boundary layer until the cloud is sufficiently thin so that the liquid water content is insufficient to maintain the instability. Likewise, there may be conditions where the cloud may have a relatively broken structure due to the ratio w_e/w^* or other cloud processes, such as precipitation, that can deplete the cloud-layer liquid water. Thus, cloud-top entrainment instability in its present form should not be viewed as a necessary and sufficient condition for the breakup of a stratocumulus cloud. (See also Mahrt and Paumier, 1982; Randall, 1984; Hanson, 1984a,b.) Other conditions may be important and more study is needed to determine how various processes affect the structure of stratocumulus clouds. The entrainment process and the associated mixing process are still not well understood. Further studies of these processes will be needed if their effects on cloud-top mixed layers are to be totally understood.

9. Conclusions

Data collected on three flights made with the NCAR Electra were used to study the mean thermodynamic structure, liquid water structure, radiative fluxes and turbulent fluxes of heat and moisture associated with cloud-topped mixed layers. The structure of the clouds studied on these three flights consisted of a relatively "thin" and somewhat broken cloud, a "broken" cloud, and a "solid" cloud. Although these clouds had different structures, they were associated with boundary layers that demonstrated the validity of assuming a well-mixed structure below the inversion. For the broken cloud case, longwave cooling clearly occurs in the cloud layer. For the solid case, the radiative cooling is observed to occur in a zone that is ~50 m below the entrainment zone at the inversion. There was some evidence that the differences in the cloud structures were due in part to cloud microphysics.

Heat and moisture fluxes were compared for the three cases. Although Brost *et al.* (1982b) determined that shear production made an important contribution to the turbulence kinetic energy budget for the broken and solid cloud cases, there is buoyancy production in the three cases studied. This study did not, however, include cases in which cloud conditions were poorly defined or nonuniform over the distance of the turbulence legs (~60 km). For the thin and broken cloud cases the buoyancy generation due to surface fluxes was significant. For the solid case there was little production at the surface but significant buoyancy production in the cloud layer. In general, the vertical distribution of the fluxes was consistent with the linear distribution assumed in the models based on Lilly's (1968) mixed-layer model. This was not true for the broken cloud case, in which the moisture flux distribution was consistent with the moistening and drying needed to balance drizzle processes.

The cloud-top entrainment instability conditions defined by Lilly (1968) and refined to include virtual effects by Deardorff (1980a) and Randall (1980b) were satisfied for the thin cloud case. There was little evidence for any realization of this instability into rapid entrainment. For the broken cloud case the instability conditions were not satisfied. The conditions required for the instability to occur were examined in more detail by considering mixtures of cloudy and unsaturated parcels. It was found that the cloud-top entrainment instability should not be applied as a necessary and sufficient condition for the breakup of stratocumulus.

Overall, the measurements support the general approach used to model stratocumulus, but clearly indicate that these models need to be generalized in order to capture the variety of cloud conditions that may exist for cloud-topped mixed layers.

Acknowledgments. We gratefully acknowledge the cooperation and support of the NCAR Research Aviation Facility during the field phase of this research. The first author appreciates the initial encouragement of Dr. D. Lilly and benefited from discussions with Drs. R. Brost, D. Lenschow, J. Deardorff, A. Betts and C. Fairall. We also wish to acknowledge the assistance provided by Karen Schuckman and Robert Lipschitz on the data reduction. This research was supported by the National Science Foundation (NSF) under Grant ATM-7915254 and the NSF and National Oceanic and Atmospheric Administration under Grant ATM-80-09307.

REFERENCES

Albrecht, B. A., and S. K. Cox, 1977: Procedures for improving pyrgeometer performance. *J. Appl. Meteor.*, **16**, 188–197.

——, —— and W. H. Schubert, 1979: Radiometric measurements of in-cloud temperature fluctuations. *J. Appl. Meteor.*, **18**, 1066–1071.

Baumgardner, D., and J. E. Dye, 1983: The 1982 cloud particle measurement symposium, 4–7 May 1982, Boulder, CO. *Bull. Amer. Meteor. Soc.*, **64**, 366–370.

Betts, A. K., 1973: Nonprecipitating cumulus convection and its parameterization. *Quart. J. Roy. Meteor. Soc.*, **99**, 178–196.

——, 1978: Convection in the tropics. *Meteorology Over the Tropical Oceans*, D. B. Shaw, Ed., Royal Meteor. Soc., 105–132.

——, 1982: Saturation point analysis of moist convective overturning. *J. Atmos. Sci.*, **39**, 1484–1505.

——, 1983: Thermodynamics of mixed stratocumulus layers: Saturation point budgets. *J. Atmos. Sci.*, **40**, 2655–2670.

Brost, A. K., D. H. Lenschow and J. C. Wyngaard, 1982a: Marine stratocumulus layers. Part I: Mean conditions. *J. Atmos. Sci.*, **39**, 800–817.

——, —— and ——, 1982b: Marine stratocumulus layers. Part II: Turbulence budgets. *J. Atmos. Sci.*, **39**, 818–836.

Caughey, S. J., B. A. Crease and W. T. Roach, 1982: A field study of nocturnal stratocumulus. II: Turbulence structure and entrainment. *Quart. J. Roy. Meteor. Soc.*, **109**, 124–144.

Chen, C., and W. R. Cotton, 1983: A one-dimensional simulation of the stratocumulus-capped mixed layer. *Bound.-Layer Meteor.*, **25**, 289–321.

Deardorff, J. W., 1976: On the entrainment rate of a stratocumulus-topped mixed layer. *Quart. J. Roy. Meteor. Soc.*, **102**, 563–582.

——, 1980a: Cloud-top entrainment instability. *J. Atmos. Sci.*, **37**, 131–147.

——, 1980b: Stratocumulus-capped mixed layers from a three-dimensional model. *Bound.-Layer Meteor.*, **18**, 495–527.

——, 1981: On the distribution of mean radiative cooling at the top of a stratocumulus-capped mixed layer. *Quart. J. Roy. Meteor. Soc.*, **107**, 191–202.

Emanuel, K. A., 1981: A similarity theory for unsaturated downdrafts within clouds. *J. Atmos. Sci.*, **38**, 1541–1557.

Fravalo, C., Y. Fouquart and R. Rosset, 1981: The sensitivity of a model of low stratiform clouds to radiation. *J. Atmos. Sci.*, **38**, 1049–1062.

Hanson, H. P., 1981: Note on stratocumulus instability. *Tellus*, **33**, 109–112.

——, 1984a: On mixed-layer modeling of the stratocumulus-topped marine boundary layer. *J. Atmos. Sci.*, **41**, 1226–1234.

——, 1984b: Stratocumulus instability reconsidered: A search for physical mechanisms. *Tellus*, **36A**, 355–368.

Kahn, P. K., and J. A. Businger, 1979: The effect of radiative flux divergence on the entrainment of a saturated convective boundary layer. *Quart. J. Roy. Meteor. Soc.*, **105**, 303–306.

Kraus, H., and E. Schaller, 1978a: Steady-state characteristics of inversions capping a well-mixed planetary boundary layer. *Bound.-Layer Meteor.*, **14**, 83–104.

——, and ——, 1978b: A note on the closure in Lilly-type inversion models. *Tellus*, **30**, 284–288.

Lenschow, D. H., and W. T. Pennell, 1974: On measurement of in-cloud and wet-bulb temperature from an aircraft. *Mon. Wea. Rev.*, **102**, 447–454.

Lilly, D. K., 1968: Models of cloud-topped mixed layers under a strong inversion. *Quart. J. Roy. Meteor. Soc.*, **94**, 292–309.

——, and W. H. Schubert, 1980: The effects of radiative cooling in cloud-topped mixed layers. *J. Atmos. Sci.*, **37**, 482–487.

Mahrt, L., and J. Paumier, 1982: Cloud-top entrainment instability observed in ATEX. *J. Atmos. Sci.*, **39**, 622–634.

Moeng, C.-H., and A. Arakawa, 1980: A numerical study of a marine subtropical stratus cloud layer and its stability. *J. Atmos. Sci.*, **37**, 2661–2676.

Nicholls, S., and LeMone, M. A., 1980: Fair weather boundary layer in GATE: The relationship of subcloud fluxes and structure to the distribution and enhancement of cumulus clouds. *J. Atmos. Sci.*, **37**, 2051–2067.

Noonkester, R. V., 1984: Droplet spectra observed in marine stratus cloud layers. *J. Atmos. Sci.*, **41**, 829–845.

Oliver, D. A., W. S. Lewellen and G. G. Williamson, 1978: The interaction between turbulent and radiative transport in the development of fog and low-level stratus. *J. Atmos. Sci.*, **35**, 301–316.

Penc, R., 1983: Heat and moisture fluxes in cloud-topped mixed layers. M.S. Thesis, Dept. of Meteorology, The Pennsylvania State University, 122 pp.

Randall, D. A., 1980a: Entrainment into a stratocumulus layer with distributed radiative heating. *J. Atmos. Sci.*, **37**, 148–159.

——, 1980b: Conditional instability of the first kind upside down. *J. Atmos. Sci.*, **37**, 125–130.

——, 1984: Stratocumulus cloud deepening through entrainment. *Tellus*, **36A**, 446–457.

Roach, W. T., R. Brown, S. J. Caughey, B. A. Grease and A. Slingo, 1982: A field study of nocturnal stratocumulus. I. Mean structure and budgets. *Quart. J. Roy. Meteor. Soc.*, **108**, 103–132.

Schaller, E., and H. Kraus, 1978: Time-dependent inversions in different climatic regions. *Beitr. Phys. Atmosphys.*, **51**, 230–246.

——, and ——, 1981a: The role of radiation in an inversion-capped planetary boundary layer. Part I: The need for detailed consideration of radiative processes. *Bound.-Layer Meteor.*, **20**, 485–495.

——, and ——, 1981b: The role of radiation in an inversion-capped planetary boundary layer. Part II: The internally interactive radiative-convective model. *Bound.-Layer Meteor.*, **20**, 497–513.

Schubert, W. H., 1976: Experiments with Lilly's cloud-topped model. *J. Atmos. Sci.*, **33**, 485–495.

——, J. S. Wakefield, E. J. Steiner and S. K. Cox, 1979a: Marine stratocumulus convection. Part I: Governing equations and horizontally homogeneous solutions. *J. Atmos. Sci.*, **36**, 1286–1307.

——, ——, —— and ——, 1979b: Marine stratocumulus convection. Part II: Horizontally inhomogeneous solutions. *J. Atmos. Sci.*, **36**, 1308–1324.

Slingo, A., R. Brown and C. L. Wrench, 1982: A field study of nocturnal stratocumulus. Part III. High resolution radiative and microphysical observations. *Quart. J. Roy. Meteor. Soc.*, **108**, 145–165.

Squires, P., 1958: Penetrative downdraughts in cumuli. *Tellus*, **10**, 381–389.

Stage, S. A., and J. A. Businger, 1981a: A model for entrainment into a cloud-topped marine boundary layer. Part I: Model description and application to a cold-air outbreak episode. *J. Atmos. Sci.*, **38**, 2213–2229.

——, and ——, 1981b: A model for entrainment into a cloud-topped marine boundary layer. Part II: Discussion of model behavior and comparison with other models. *J. Atmos. Sci.*, **39**, 2230–2242.

Wakefield, J. S., and W. H. Schubert, 1976: Design and execution of the marine stratocumulus experiment. Atmos. Sci. Paper No. 256, Department of Atmospheric Science, Colorado State University, Fort Collins, CO.

——, and ——, 1981: Mixed-layer model simulation of eastern North Pacific stratocumulus. *Mon. Wea. Rev.*, **109**, 1952–1968.